The Astrophysical Journal, 853:62 (16pp), 2018 January 20 https://doi.org/10.3847/1538-4357/aaa014

The Early Detection and Follow-up of the Highly Obscured Type II Supernova 2016ija/DLT16am*

L. Tartaglia[1,2], D. J. Sand[1], S. Valenti[2], S. Wyatt[1], J. P. Anderson[3], I. Arcavi[4,5,30], C. Ashall[6], M. T. Botticella[7], R. Cartier[8], T.-W. Chen[9], A. Cikota[10], D. Coulter[11], M. Della Valle[7], R. J. Foley[11], A. Gal-Yam[12], L. Galbany[13], C. Gall[14], J. B. Haislip[15], J. Harmanen[16], G. Hosseinzadeh[4,5], D. A. Howell[4,5], E. Y. Hsiao[17], C. Inserra[8], S. W. Jha[18], E. Kankare[19], C. D. Kilpatrick[11], V. V. Kouprianov[15], H. Kuncarayakti[16,20], T. J. Maccarone[21], K. Maguire[19], S. Mattila[16], P. A. Mazzali[6,22], C. McCully[4,5], A. Melandri[23], N. Morrell[24], M. M. Phillips[24], G. Pignata[25,26], A. L. Piro[27], S. Prentice[6], D. E. Reichart[15], C. Rojas-Bravo[11], S. J. Smartt[19], K. W. Smith[19], J. Sollerman[28], M. D. Stritzinger[29], M. Sullivan[8], F. Taddia[28], and D. R. Young[19]

[1] Department of Astronomy and Steward Observatory, University of Arizona, 933 N Cherry Avenue, Tucson, AZ 85719, USA; ltartaglia@ucdavis.edu
[2] Department of Physics, University of California, 1 Shields Avenue, Davis, CA 95616, USA
[3] European Southern Observatory, Alonso de Córdova 3107, Casilla 19, Santiago, Chile
[4] Department of Physics, University of California, Santa Barbara, CA 93106-9530, USA
[5] Las Cumbres Observatory, 6740 Cortona Drive, Suite 102, Goleta, CA 93117, USA
[6] Astrophysics Research Institute, Liverpool John Moores University, IC2, Liverpool Science Park, 146 Brownlow Hill, Liverpool L3 5RF, UK
[7] INAF—Osservatorio Astronomico di Capodimonte, Salita Moiariello 16, Napoli, I-80131 Italy
[8] School of Physics and Astronomy, University of Southampton, Southampton, SO17 1BJ, UK
[9] Max-Planck-Institut für Extraterrestrische Physik, Giessenbachstraße 1, D-85748, Garching, Germany
[10] European Southern Observatory, Karl-Schwarzschild-Str. 2, D-85748 Garching b. München, Germany
[11] Department of Astronomy and Astrophysics, University of California, Santa Cruz, CA 95064, USA
[12] Benoziyo Center for Astrophysics, Faculty of Physics, Weizmann Institute of Science, Rehovot 76100, Israel
[13] PITT PACC, Department of Physics and Astronomy, University of Pittsburgh, Pittsburgh, PA 15260, USA
[14] Dark Cosmology Centre, Niels Bohr Institute, University of Copenhagen, Juliane Maries Vej, 30, DK-2100 Copenhagen, Denmark
[15] Department of Physics and Astronomy, University of North Carolina at Chapel Hill, Chapel Hill, NC 27599, USA
[16] Tuorla Observatory, Department of Physics and Astronomy, University of Turku, Väisäläntie 20, FI-21500 Piikkiö, Finland
[17] Department of Physics, Florida State University, Keen Building 616, Tallahasee, FL 3206-4350, USA
[18] Department of Physics and Astronomy, Rutgers, the State University of New Jersey, 136 Frelinghuysen Road, Piscataway, NJ 08854, USA
[19] Astrophysics Research Centre, School of Mathematics and Physics, Queen's University Belfast, Belfast BT7 1NN, UK
[20] Finnish Centre for Astronomy with ESO (FINCA), University of Turku, Väisäläntie 20, 21500 Piikkiö, Finland
[21] Department of Physics, Texas Tech University, Box 41051, Lubbock, TX 79409-1051, USA
[22] Max-Planck-Institut für Astrophysik, Karl-Schwarzschild-Str. 1, D-85748 Garching bei München, Germany
[23] INAF—Osservatorio Astronomico di Brera, via E. Bianchi 36, I-23807 Merate (LC), Italy
[24] Carnegie Observatories, Las Campanas Observatory, Casilla 601, La Serena, Chile
[25] Departamento de Ciencias Fisicas, Universidad Andres Bello, Avda. Republica 252, Santiago, Chile
[26] Millennium Institute of Astrophysics (MAS), Nuncio Monseor Stero Sanz 100, Providencia, Santiago, Chile
[27] The Observatories of the Carnegie Institution for Science, 813 Santa Barbara Street, Pasadena, CA 91101, USA
[28] Department of Astronomy and The Oskar Klein Centre, AlbaNova University Center, Stockholm University, SE-106 91 Stockholm, Sweden
[29] Department of Physics and Astronomy, Aarhus University, Ny Munkegade 120, DK-8000 Aarhus C, Denmark
Received 2017 October 6; revised 2017 December 3; accepted 2017 December 5; published 2018 January 23

Abstract

We present our analysis of the Type II supernova DLT16am (SN 2016ija). The object was discovered during the ongoing $D < 40$ Mpc (DLT40) one-day cadence supernova search at $r \sim 20.1$ mag in the "edge-on" nearby ($D = 20.0 \pm 4.0$ Mpc) galaxy NGC 1532. The subsequent prompt and high-cadenced spectroscopic and photometric follow-up revealed a highly extinguished transient, with $E(B - V) = 1.95 \pm 0.15$ mag, consistent with a standard extinction law with $R_V = 3.1$ and a bright ($M_V = -18.48 \pm 0.77$ mag) absolute peak magnitude. A comparison of the photometric features with those of large samples of SNe II reveals a fast rise for the derived luminosity and a relatively short plateau phase, with a slope of $S_{50V} = 0.84 \pm 0.04$ mag/50 days, consistent with the photometric properties typical of those of fast-declining SNe II. Despite the large uncertainties on the distance and the extinction in the direction of DLT16am, the measured photospheric expansion velocity and the derived absolute V-band magnitude at ~50 days after the explosion match the existing luminosity–velocity relation for SNe II.

Key words: galaxies: individual (NGC 1532) – supernovae: general – supernovae: individual (SN 2016ija, DLT16am)

Supporting material: data behind figure, machine-readable tables

1. Introduction

The study of cosmic explosions continues to flourish, with innovative experiments exploring new regions of discovery space. Many of these programs are focusing on wide-field imaging and relatively short cadences; see, e.g., the Palomar Transient Factory (PTF; Law et al. 2009;), the Asteroid Terrestrial-impact Last Alert System (Tonry 2011), the All Sky Automated Survey for SuperNovae (Shappee et al. 2014; Kochanek et al. 2017), and the PANoramic Survey Telescope And Rapid Response System (Pan-STARRS1; Chambers et al. 2016) among others. These programs discover hundreds

* This paper includes data gathered with the 6.5 m *Magellan* Telescopes located at Las Campanas Observatory, Chile.
[30] Einstein Fellow.

of new supernovae (SNe) every year. This revolution will certainly continue in the era of the Zwicky Transient Facility (Bellm 2014), BlackGEM[31] (Bloemen et al. 2015), and the Large Synoptic Survey Telescope (Ivezic et al. 2008). It is still the case, however, that the nearest SNe are not always caught soon after explosion, relinquishing the opportunity for detailed study of the most observable events—a recent prominent example was the type Ia SN 2014J in M82 ($D \sim 3.5$ Mpc), which was discovered ∼8 days after explosion (Fossey et al. 2014; Goobar et al. 2015).

It is in the hours to days after explosions where clues about the SN progenitors and explosion physics are accessible, and where the fewest observational constraints are present. Early discovery and prompt multi-wavelength follow-up of nearby SNe are essential to fully characterize the physical properties of stellar explosions. Except for a few cases where deep archival *Hubble Space Telescope (HST)* images are available (Smartt 2009), one of the best ways to gain insight into a SN progenitor and its explosion mechanism is through the analysis of very early-phase data, when the spectra still show the imprint from the outer layers of the progenitor, the explosion energy is still the dominant heat source, and the circumstellar medium (CSM) has not yet been overtaken by the SN ejecta.

In SNe Ia, the very early light curves and spectra can help to constrain the white dwarf (WD) progenitor radius (e.g., Nugent et al. 2011; Bloom et al. 2012; Zheng et al. 2013), its ^{56}Ni distribution (from the early light curve shape; see Mazzali et al. 2014; Piro & Nakar 2014; Miller et al. 2017), to infer the presence of a normal companion star (via direct shocking of the SN Ia ejecta against the normal companion Kasen 2010; Cao et al. 2015; Marion et al. 2016; Hosseinzadeh et al. 2017), and to probe SN Ia explosion mechanisms. While it is commonly accepted that SNe Ia arise from thermonuclear explosions of carbon-oxygen WDs, it is still unclear by which mechanism(s) the WD accretes the necessary mass (the single or double degenerate scenario; see, e.g., Maoz & Mannucci 2012 for a review). The detection and strength of C II (6580 Å) in early spectra may also point to viable explosion mechanisms (see, e.g., Mazzali 2001; Höflich & Stein 2002; Röpke et al. 2007; Kasen et al. 2009; Fryer et al. 2010).

Early light curves of core-collapse (CC) SN shock-cooling tails can constrain the progenitor star radius and give useful information about the envelope structure (see, e.g., Rabinak & Waxman 2011; Bersten et al. 2012; Arcavi et al. 2017; Barbarino et al. 2017; Piro et al. 2017; Sapir & Waxman 2017, for selected theoretical and observational results). Alternatively, "flash spectroscopy" at very early phases can probe the physical properties of the CSM as well as the mass-loss history of the progenitor star prior to its explosion (e.g., Gal-Yam et al. 2014; Smith et al. 2015; Khazov et al. 2016; Yaron et al. 2017). Even when archival *HST* data are available, radius estimates through the analysis of very early data can give important results, since the progenitor field might be contaminated by the presence of binary companions (e.g., Tartaglia et al. 2017a).

Motivated by the science described above, and by the need for multi-wavelength observations at very early phases, we have begun a pointed, one-day cadence SN search for very young transients in the nearby ($D < 40$ Mpc; DLT40) universe. Given the survey depth of $r \simeq 19$ mag and the proximity of the DLT40 galaxy sample (see Section 2), this program is also sensitive to heavily extinguished SNe. A significant number of CCSNe are likely missed by current optical surveys, even in normal nearby galaxies due to dust extinction (Mattila et al. 2012; Jencson et al. 2017), which may explain the unexpectedly low CCSNe rate with respect to the cosmic star formation rate (SFR; Horiuchi et al. 2011; Dahlen et al. 2012; Melinder et al. 2012; Cappellaro et al. 2015; Strolger et al. 2015).

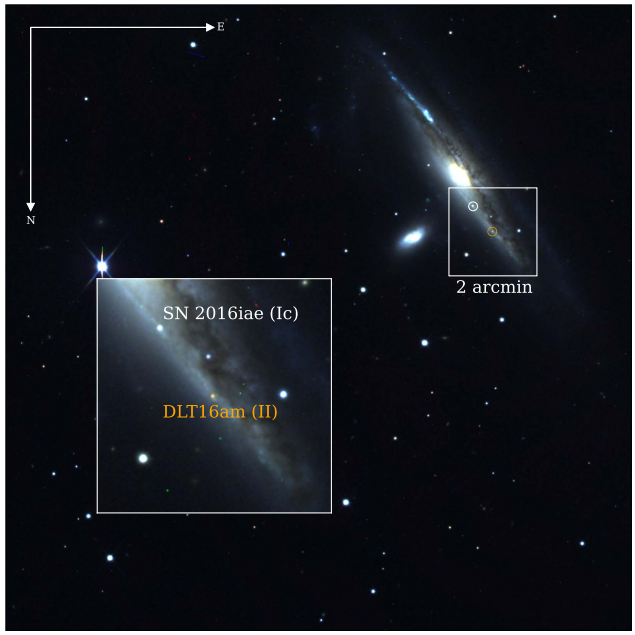

Figure 1. RGB images of the DLT16am field obtained using *i*-, *r*-, and *g*-band images, respectively. The position of the Type Ic SN 2016iae is marked for reference. A zoomed-in view of the region of the two SNe is shown in the inset (∼2′).

In this paper we describe the highly obscured, nearby Type II SN DLT16am (SN 2016ija), the first SN discovered by the DLT40 supernova search. DLT16am was discovered on 2016 November 21.19 UT (Tartaglia et al. 2016b) in the nearby galaxy NGC 1532 (see Figure 1). Fortuitously, the type Ic SN 2016iae (S. Prentice et al. 2017, in preparation) was discovered in the same galaxy ∼2 weeks before and was being observed by a number of groups, allowing very tight constraints on the explosion time of DLT16am itself (JD = 2457712.6 ± 1.0 days, see Section 5). The SN is located at R.A. = 04:12:07.64, decl. = −32:51:10.57 [J2000], 42.″08 E, 76.″43 N offset from the center of NGC 1532. It was first suggested to be a 91T-like SN Ia, showing a nearly featureless and very red continuum, although subsequent early spectra revealed broad Hα and calcium features on top of a red continuum, leading to a more appropriate classification as a highly reddened SN II[32]. DLT16am is heavily extinguished, but we were still able to obtain a comprehensive multi-wavelength data set, allowing a detailed comparison of its properties with standard, less extinguished SNe II.

This paper is organized as follows. Section 2 is a description of the DLT40 survey, while Section 3 describes the instrumental setups and the reduction tools used to carry out the follow-up campaign of DLT16am. In Section 4 we present the results of our analysis on the host galaxy, NGC 1532.

[31] https://astro.ru.nl/blackgem/

[32] https://wis-tns.weizmann.ac.il/object/2016ija

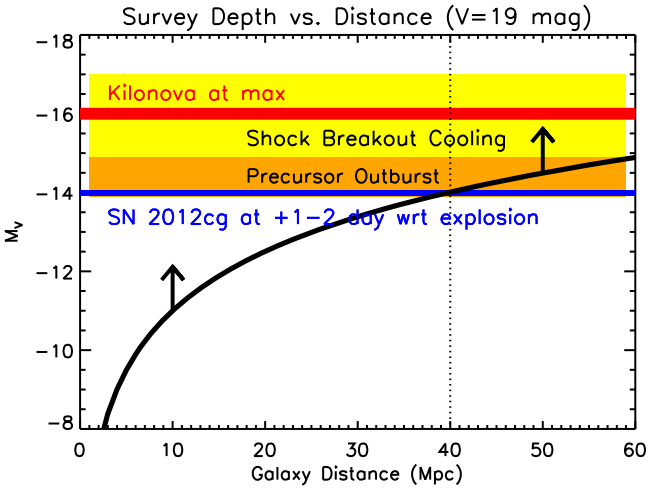

Figure 2. Absolute magnitude reached for a survey depth of $V = 19$ mag as a function of distance (black line); note that a survey like DLT40 is sensitive to the region above the black solid line. Also noted is the absolute magnitude of SN 2012cg, ∼1–2 days after explosion, which has possible early-time light curve features that can shed light on the progenitor (Marion et al. 2016). We also plot the the *V*-band absolute magnitude of the kilonova DLT17ck (AT 2017gfo) at maximum (Valenti et al. 2017a).

Sections 5 and 6 report the main results of our photometric and spectroscopic analysis, respectively, while in Section 7 we compare the main spectroscopic and photometric features of DLT16am with those displayed by other SNe II. Finally, we summarize our results in Section 8.

2. The DLT40 Survey

The goal of DLT40 is not to find many SNe, but ∼10 nearby SNe per year within ∼1 day from explosion. Fully operational since late summer 2016, we observe ∼300–600 galaxies per night using a PROMPT 0.4 m telescope (PROMPT5; Reichart et al. 2005) at the Cerro Tololo Inter-American Observatory (CTIO), achieving a typical single-epoch depth of $r \approx 19$–20 mag with filterless observations and a 45 s integration time.

The field of view of 10×10 arcmin^2 is sufficient to completely image all but the nearest galaxies. DLT40 is sensitive to most of the early observational signatures that can be used to constrain the nature of the progenitor stars, as illustrated in Figure 2.

The DLT40 galaxy sample is drawn from the nearby Gravitational Wave Galaxy Catalog of White et al. (2011). From this list, we select all potential DLT40 galaxies with $M_B < -18$ mag, Milky Way (MW) extinction $A_V < 0.5$ mag and recessional velocity $v_r < 3000$ km s^{-1}, corresponding to a Hubble flow distance of $D \lesssim 40$ Mpc. Our nightly schedule is based on this list, with preference given to those fields observed in the previous three days, along with intrinsically bright ($M_B < -20$ mag) or nearby galaxies ($D < 11$ Mpc) and fields that have more than one target galaxy within the PROMPT field of view. Given the high SFRs and stellar masses of our targets, and based on current SN rates and simulations, we expect to find ∼20 SN yr^{-1}. Assuming some weather and instrument problems, we ultimately expect ∼10 SN yr^{-1} (∼2–3 Ia, ∼2–3 Ib/c, and ∼4–5 SNe II per year) discovered within ∼1 day of explosion. PROMPT5 DLT40 pre-reduced images are delivered within ∼1 minute of the data being taken, and are further processed by our pipeline, which includes quality checks, difference imaging (with HOTPANTS; Becker 2015), candidate detection and scoring (based on the difference image properties), databasing and web site generation of stamps for candidate inspection. The average lag between an observation and the visualization of the SN candidates is ∼3–4 minutes, after which one or more team members can immediately trigger a PROMPT5 confirmation image or further observations at other facilities.

First results from the DLT40 survey were presented for the nearby Type Ia SN 2017cbv (DLT17u; Hosseinzadeh et al. 2017) and for the kilonova DLT17ck (AT 2017gfo Valenti et al. 2017a). Additionally, an upper limit on the rate of fast kilonova-like events was calculated from the first year of DLT40 data (Yang et al. 2017). Thirteen discoveries have been reported to the Astronomer's Telegram service (Tartaglia et al. 2016a, 2017b, 2017c, 2017d, 2017e, 2017f, 2017g, 2017h, 2017i; Sand et al. 2017a, 2017b; Valenti et al. 2017b), in line with our initial expectations. More DLT40 results are in preparation.

3. Observations and Data Reduction

3.1. Spectra

The spectral sequence of DLT16am is shown in Figure 3, while the log of the spectroscopic observations in the optical and NIR domains is reported in Table 1. Optical spectra were mainly provided by Public ESO Spectroscopic Survey for Transient Objects (PESSTO) using the ESO 3.58 m New Technology Telescope (NTT) with the ESO Faint Object Spectrograph and Camera (v.2, EFOSC2; Buzzoni et al. 1984), and the Las Cumbres Observatory network of telescopes, using the 2 m Faulkes north and south telescopes with FLOYDS (reduced as in Valenti et al. 2014). Early-phase spectra were also provided using the 10 m South African Large Telescope (SALT) with the Robert Stobie Spectrograph (RSS), and the 2.56 m Nordic Optical Telescope (NOT) with Andalucia Faint Object Spectrograph and Camera (ALFOSC). NOT spectra were reduced using FOSCGUI, while the SALT spectrum was reduced using a dedicated pipeline (PYSALT; Crawford et al. 2010).

NIR spectra were obtained using the standard "ABBA" technique and an A0V telluric standard was observed at a similar airmass in order to simultaneously correct for telluric absorption and to flux-calibrate the main science data. Most NIR spectra were provided by PESSTO using the NTT with the SOFI spectrograph (all reduced as in Smartt et al. 2015). Two NIR spectra were obtained using the Gemini NIR Spectrograph (GNIRS) at Gemini North (Elias et al. 2006) in cross-dispersed mode, using the 32 l mm^{-1} grating and the 0.″675 slit. This setup yields continuous wavelength coverage from 0.8 to 2.5 μm with a resolution of $R \sim 1000$. The data were taken with the slit along the parallactic angle, and were reduced with the XDGNIRS PYRAF-based pipeline provided by Gemini Observatory. Flux calibration and telluric correction were performed following the methodology of Vacca et al. (2003). An NIR spectrum was also obtained using the 6.5 m *Magellan* Baade Telescope with the Folded-port InfraRed Echellette (FIRE). The spectrum was taken in the long slit prism mode, 0.″6 slit width, and was a combination of 8 exposures of 126.8 s each. The reduction was done using the standard "firehose" IDL package (Simcoe et al. 2013).

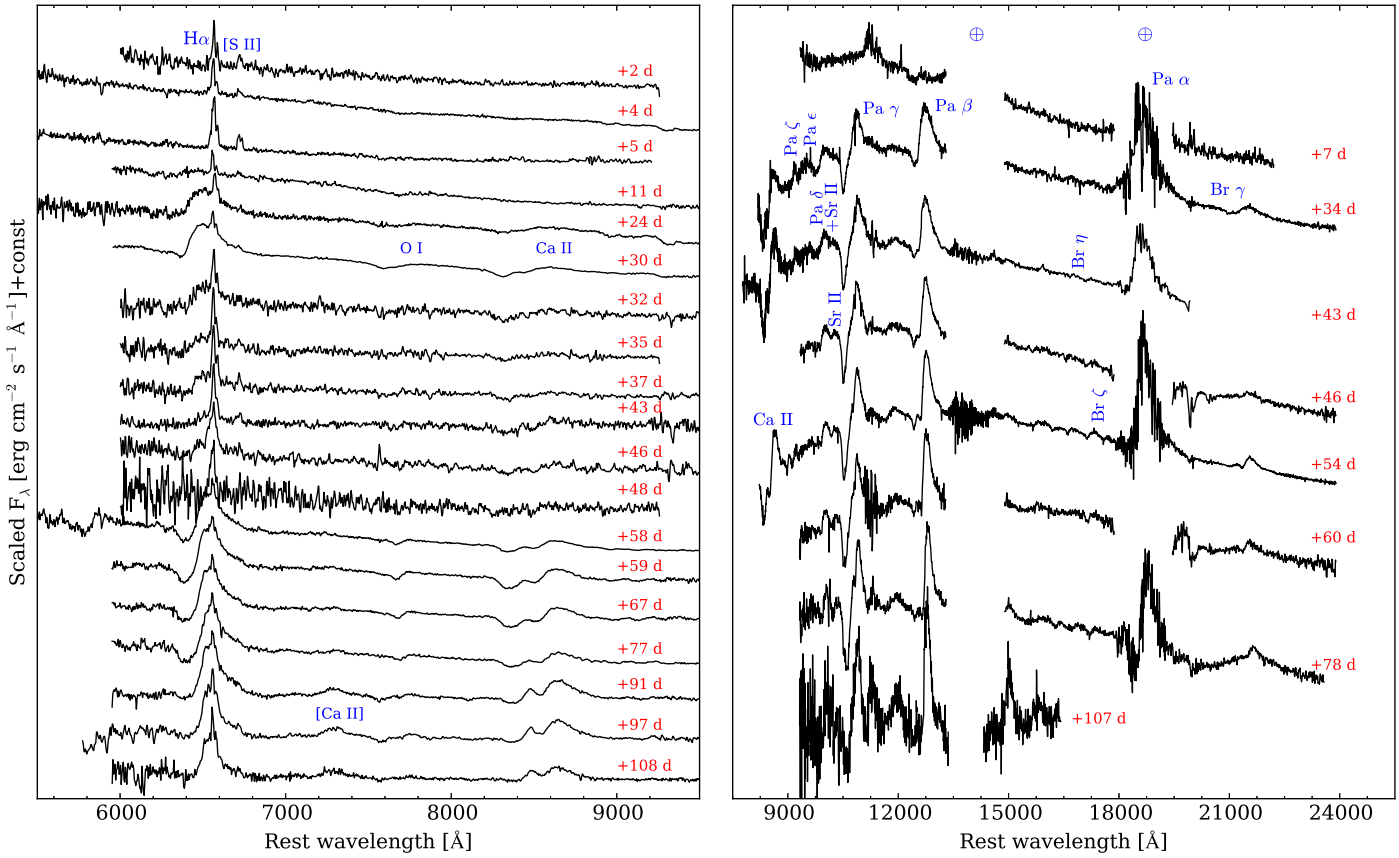

Figure 3. Left: Optical. Right: NIR spectral sequence of DLT16am. The phases refer to the epoch of the explosion. ⊕ symbols mark the positions of the main absorption telluric features. Optical spectra have been corrected for total extinction and redshift. The positions of the main lines are marked. NIR spectra have not been corrected for the total extinction to highlight shallower spectroscopic features.
(The data used to create this figure are available.)

Multi-wavelength (300–2500 nm) intermediate resolution spectra were obtained using the ESO Very Large Telescope (VLT) with X-shooter (Vernet et al. 2011), mounted at the Cassegrain focus of the 8 m VLT UT2 telescope. UVB, VIS, and NIR arm data (covering the 300–559.5, 559.5–1024 and 1024–2480 nm wavelength ranges, respectively) were reduced using the X-shooter dedicated pipeline through the ESOREFLEX environment (Freudling et al. 2013).

Optical and NIR spectra will be released through the Weizmann Interactive Supernova data REPository (WISEREP[33]; Yaron & Gal-Yam 2012).

3.2. Light Curves

Photometric data are shown in Figure 4 and reported in Tables 2–4, including publicly available early-time photometry (Chen et al. 2016; Smith et al. 2016).

The *griz* data were mainly provided by the Las Cumbres Observatory (Brown et al. 2013). Additional *griz* data were obtained using the MPG/ESO 2.2 m telescope at the La Silla Observatory with the Gamma-ray Burst Optical/Near-infrared Detector (GROND; Greiner et al. 2008), which also provided early-phase photometric data at near-infrared (NIR) wavelengths; the 2 m Liverpool Telescope with the optical imaging component of the Infrared-Optical camera (IO:O); the 2.56 m NOT with the ALFOSC, and the Las Campanas Observatory 1 m Swope Telescope with an E2V camera (Bowen & Vaughan 1973). Pre-reduction steps (including bias, flat-field corrections, image-stacking, and astrometry calibration) for GROND frames were performed as in Krühler et al. (2008), while the final magnitudes for the GROND, IO:O, ALFOSC, and Swope frames were obtained using the reduction pipeline SNOoPy.[34] All these images were template-subtracted and photometry was calibrated to the AAVSO Photometric All-Sky Survey (APASS[35]) catalog.

DLT16am was also observed in the framework of the CHilean Automatic Supernova sEarch survey (Pignata et al. 2009) in Johnson-Cousins *R* filters using the PROMPT1 telescope (Reichart et al. 2005). All images were reduced following standard procedures, including dark (with the same exposure time) and flat-field corrections, and then they were template-subtracted. The computed photometry is relative to a local sequence calibrated in the field of NGC 1532. The PROMPT1 Johnson-Cousins *R*-band magnitudes were transformed to the Sloan *r*-band following the procedure reported in Pignata et al. (2008).

Unfiltered data were provided by the DLT40 (see Section 2) SN search using the 0.4 m PROMPT5 telescope (Reichart et al. 2005), template-subtracted, and calibrated to the APASS *r*-band.

DLT16am exploded in the same host and ∼2 weeks after the Type Ic SN 2016iae (Jha et al. 2016), and pre-SN *V*-band

[33] https://wiserep.weizmann.ac.il/

[34] http://sngroup.oapd.inaf.it/snoopy.html

[35] https://www.aavso.org/apass

Table 1
Log of the Spectroscopical Observations

Date (UT)	JD	Phase (day)	Instrumental Setup	Grism/Grating	Spectral Range (Å)	Exposure Time (s)
20161122	2457715.144	+2	FTS+FLOYDS	235 l/mm	5000 − 9200	3600
20161123	2457716.557	+4	NOT+ALFOSC	Gr4	4000–9700	2400
20161124	2457717.315	+5	SALT+RSS	PG0300	3300–9200	2326
20161127	2457719.735	+7	ESO NTT+SOFI	GB+GR	9000–22000	8 × 270 + 8 × 450
20161201	2457723.753	+11	ESO NTT+EFOSC2	Gr16	6000–10000	2700
20161213	2457736.516	+24	NOT+ALFOSC	Gr4	4000–9700	2400
20161219	2457742.732	+30	ESO NTT+EFOSC2	Gr16	6000–10000	2700
20161222	2457744.517	+32	ESO VLT+X-shooter	UVB+VIS+NIR	3500–25000	700 + 600 + 600
20161222	2457744.881	+32	FTN+FLOYDS	235 l/mm	5000–9200	3600
20161224	2457746.568	+34	Gemini+GNIRS	ShortXD	8800–24000	3000
20161225	2457747.846	+35	FTN+FLOYDS	235 l/mm	5000–9200	3600
20161227	2457749.842	+37	FTN+FLOYDS	235 l/mm	5000–9200	3600
20170102	2457755.671	+43	Baade+FIRE	LDPrism	8800–20000	8 × 126.8
20170102	2457756.019	+43	FTS+FLOYDS	235 l/mm	5000–9200	3600
20170104	2457758.693	+46	ESO NTT+SOFI	GB+GR	9000–24000	8 × 270 + 8 × 450
20170105	2457758.945	+46	FTS+FLOYDS	235 l/mm	5000–9200	3600
20170107	2457760.928	+48	FTS+FLOYDS	235 l/mm	5000–9200	3600
20170113	2457766.815	+54	Gemini+GNIRS	ShortXD	8800–24000	3000
20170116	2457770.386	+58	NOT+ALFOSC	Gr4	4000–9700	2400
20170117	2457771.620	+59	ESO NTT+EFOSC2	Gr16	6000–10000	2400
20170118	2457772.620	+60	ESO NTT+SOFI	GB+GR	9000–24000	8 × 270 + 8 × 450
20170125	2457779.635	+67	ESO NTT+EFOSC2	Gr16	6000–10000	2400
20170204	2457789.619	+77	ESO NTT+EFOSC2	Gr16	6000–10000	2700
20170206	2457790.591	+78	ESO NTT+SOFI	GB+GR	9000–24000	6 × 270 + 6 × 450
20170219	2457803.559	+91	ESO NTT+EFOSC2	Gr16	6000–10000	2700
20170224	2457809.554	+97	ESO NTT+EFOSC2	Gr16	6000–10000	2700
20170307	2457819.580	+107	ESO NTT+SOFI	GB	9000–17000	6 × 270
20170307	2457820.510	+108	ESO NTT+EFOSC2	Gr16	6000–10000	2700

Note. FTN: 2 m Faulkes Telescope North, Las Cumbres Observatory node at the Haleakala Observatory, Hawaii; FTS: 2 m Faulkes Telescope South, Las Cumbres Observatory node at the Siding Spring Observatory, Australia; NOT: 2.56 m Nordic Optical Telescope, located at Roque de los Muchachos, La Palma, Spain; ESO VLT: 8.2 m Very Large Telescope, located at the ESO Cerro Paranal Observatory, Chile; ESO NTT: 3.58 m New Technology Telescope, located at the ESO La Silla Observatory, Chile; Baade: 6.5 m *Magellan* (Walter Baade) Telescope at the Las Campanas Observatory, Chile; Gemini: 8.19 m Gemini North Telescope at the Mauna Kea Observatories, Hawaii.

acquisition images of the field were obtained during its PESSTO spectroscopic campaign. These data were used to constrain the explosion epoch and are included in the *V*-band light curve of DLT16am (see Smith et al. 2016 and Section 5).

JHK data were also provided by PESSTO[36] using the 3.58 m NTT with the Son Of ISAAC camera (SOFI; Moorwood et al. 1998) and reduced using their dedicated pipeline (see Smartt et al. 2015). Further NIR photometry was provided by the NOT Unbiased Transient Survey (NUTS[37]) with the NOT near-infrared Camera and spectrograph (NOTCam). Pre-reduction steps for NOTCam data were obtained with a modified version of the external IRAF package NOTCAM (v.2.5).[38] In addition to differential flat-fielding and median sky level correction, a bad pixel masking and distortion correction were applied before stacking dithered images. Magnitudes were obtained from pre-reduced images using a dedicated pipeline (FOSCGUI[39]). NIR photometry was calibrated to the Two Micron All-Sky Survey[40] catalog, through point-spread-function (PSF) fitting techniques.

[36] http://www.pessto.org
[37] http://csp2.lco.cl/not/
[38] http://www.not.iac.es/instruments/notcam/guide/observe.html #reductions.
[39] http://sngroup.oapd.inaf.it/foscgui.html
[40] https://www.ipac.caltech.edu/2mass/

DLT16am was also observed with *Swift*/XRT on 2016 November 25 (for 2889.4 s), November 26 (for 2966.8 s), November 28 (for 1023.9 s), and December 1 (for 2936.8 s). A previous *Swift*/XRT exposure of SN 2016iae (which is in the same galaxy) was used to extract the background in the region of DLT16am. Due to this complicated background, we obtained a limiting count rate (assuming an 18″ radius) of 1.67×10^{-3} counts s^{-1}. Assuming a power-law model with a photon index of 2 and a Galactic absorption 1.58×10^{20} cm^{-2} (Kalberla et al. 2005), this corresponds to an unabsorbed flux $<4.1 \times 10^{-14}$ erg cm^{-2} s^{-1} (0.4–5 keV) and an approximate luminosity of $<1.9 \times 10^{39}$ erg s^{-1} at 20 Mpc (see Section 4). We could not detect DLT16am in UVOT frames, due to the high extinction in the direction of DLT16am (see Section 4.1).

4. The Host Galaxy

NGC 1532, the host of DLT16am, is a SB(s)b edge-on galaxy (de Vaucouleurs et al. 1991), located at R.A. = 04:12:04.3, decl. = −32:52:27 [J2000], with an apparent total magnitude of $B = 10.65 \pm 0.09$ mag (Lauberts et al. 1989), showing prominent dust lanes close to the position of DLT16am. From our X-shooter spectrum obtained on 2016 December 22, we infer an heliocentric velocity of 1367 km s^{-1} ($z = 0.00456$, see Section 6.1), estimated from the average positions of the Balmer emission lines. Throughout

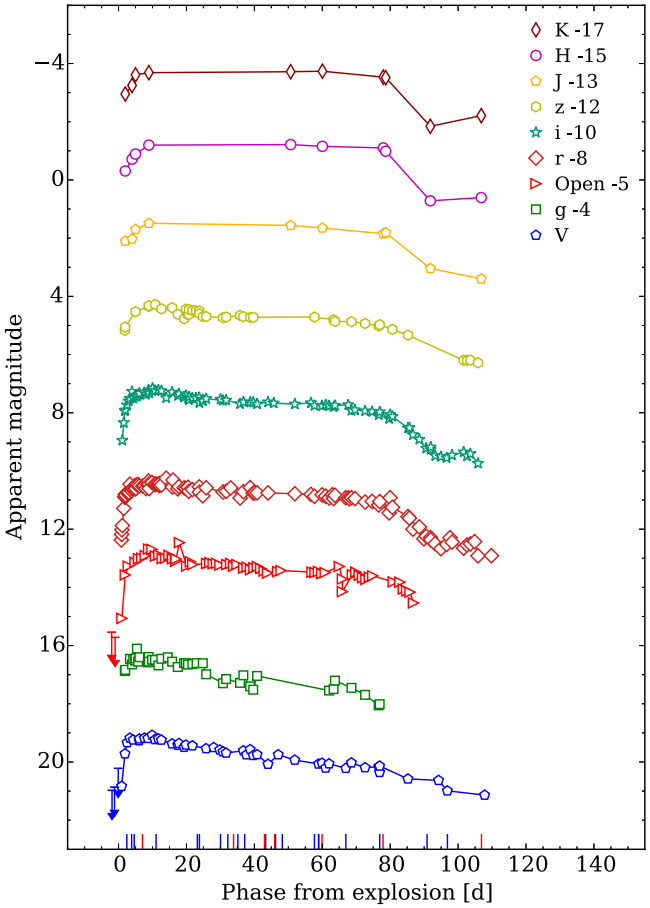

Figure 4. Multi-band light curves of DLT16am from the optical to the NIR. The blue ticks mark the epochs at which optical spectra were obtained, while the red ticks mark those of the NIR spectra. *BVJHK* and *griz* magnitudes were calibrated to the Vega and to the AB photometric system, respectively. The phases refer to the estimated epoch of the explosion (see Sections 1 and 5 for details). Magnitudes were not corrected for MW or host extinction. Main pre-discovery limits are reported for *V*-band and unfiltered light curves.

the paper we will adopt a distance of 20.0 ± 4.0 Mpc (Tully et al. 2013) to NGC 1532 (leading to a projected distance of ≃8.4 kpc from the center of the host for DLT16am). In Section 7, we will show that this value, along with the derived extinction (see Section 4.1), gives absolute magnitudes, pseudo-bolometric luminosities, and hence an estimated ^{56}Ni mass consistent with other distance-independent and reddening-independent quantities.

4.1. Extinction Estimate

While for the foreground Galactic extinction we assumed $A_V = 0.042$ mag, as derived from the Schlafly & Finkbeiner (2011) IR-based dust map, the determination of the host-reddening in the direction of DLT16am proved to be more complicated. Early spectra of DLT16am exhibit a very red continuum, with low or almost no signal at wavelengths <6000 Å (with the exception of very early phases, $T \lesssim 5$ days; see Section 6.1), a signature of very high reddening in the direction of the transient.

In order to get an estimate of the host-galaxy-reddening, we measured the equivalent widths (EWs) of the Na ID doublet in our X-shooter spectrum (see Figure 5), on the basis of the correlation between the strength of the Na ID λλ5890, 5896 absorption and the color excess (see Poznanski et al. 2012; Phillips et al. 2013).

The estimated values ($EW_{D1} \simeq 1.7$ Å, $EW_{D2} \simeq 2.5$ Å) are significantly larger than the saturation limit, where the relation flattens (EW $\gtrsim 0.2$ Å; see Poznanski et al. 2012). We therefore estimated the reddening by matching the colors of DLT16am, during the plateau phase, with those of other SNe II (i.e., SNe 2013ej, 2013ab, 2013by and 2014cx; Valenti et al. 2014, 2015; Bose et al. 2015; Huang et al. 2016, respectively; see Figure 6). These transients were selected among those with similar plateau lengths and observed using similar filters, and for the same reasons, are used throughout the paper as comparison objects.

During the plateau phase, the outer hydrogen layer starts to recombine as its temperature decreases to ∼6000 K, until the recombination front reaches its base and the plateau ends. This recombination temperature of hydrogen is relatively insensitive to density and metallicity and hence during the plateau SNe II typically share similar physical conditions (see, e.g., Schmidt et al. 1992). A scatter in their colors may therefore be attributed to extinction rather than other intrinsic behaviors (see, e.g., Faran et al. 2014b, and references therein). We therefore fitted the color excess $E(B-V)$ to match the available colors ($g-r$, $r-i$, $V-r$, and $V-i$) of the comparison objects (hereafter "references") within the plateau phase, after correcting the observed colors of the references for the corresponding total extinction. A set of values was obtained comparing the colors of DLT16am to those of each reference, taking the minima of the χ^2 distributions obtained for each color (i.e., $\chi^2 = \sum_k \frac{1}{\sigma_k^2}(\mathrm{col}_{k,\mathrm{ref}} - \mathrm{col}_{k,\mathrm{DLT16am}})^2$, where σ_k^2 are the errors on the colors of DLT16am, and $k = g-r$, $r-i$, $V-r$, $V-i$). We also accounted for the uncertainties on the photometry of the references through Monte Carlo simulations, randomly shifting the colors within their errors.

Different extinction laws were recently proposed after analyzing heavily extinguished objects (see, e.g., the case of the obscured Type Ia SN 2002cv Elias-Rosa et al. 2008). Following Calzetti et al. (2000), we also tested their proposed extinction law with $R_V = 4.05 \pm 0.80$, getting a reasonable fit to the colors of the references, but unusual bright absolute peak magnitudes for DLT16am ($M_V = -18.84 \pm 0.77$ mag), although still within the combined errors on the reddening and distance. For this reason, we cannot rule out a different extinction law for the environment of DLT16am, although we remark that changing R_V did not significantly improve the result of the fit. Hereafter, we will therefore adopt a standard value ($R_V = 3.1$; Cardelli et al. 1989). Averaging the best-fit values obtained using the different references we find $E(B-V) = 1.95 \pm 0.15$ mag. A comparable value was obtained measuring the Balmer decrement (i.e., $E(B-V) \simeq 2.0$ mag through the $H\alpha/H\beta$ flux ratio) from our X-shooter spectrum, assuming a case B recombination ratio and a standard extinction law with $R_V = 3.1$ (see, e.g., Botticella et al. 2012).

In Figure 6 we show the resulting color evolution and absolute magnitudes of DLT16am, compared with those of the references. We find color evolutions comparable with those of the models, while DLT16am shows brighter absolute magnitudes than those displayed by other objects (but similar to those observed in SN 2013by). In Section 7 we will show that the derived absolute magnitude is consistent with the photospheric

Table 2
BV and Unfiltered Light Curves of DLT16am

Date	JD	Phase (day)	*B*(err) (mag)	*V*(err) (mag)	Open(err) (mag)	Inst
20161117	2457709.590	−3.01	>19.8	>20.6	⋯	IO:O
20161117	2457710.070	−2.53	>20.2	>19.9	⋯	1m0-03
20161118	2457710.679	−1.92	⋯	⋯	>20.5	PROMPT5
20161118	2457710.780	−1.82	⋯	>21.0	⋯	EFOSC2
20161118	2457711.285	−1.31	>20.8	>20.5	⋯	1m0-10

Note. PROMPT5: 0.41 m PROMPT5 telescope at the Cerro Tololo Inter-American Observatory, Chile; EFOSC2: 3.58 m ESO New Technology Telescope with EFOSC2 at the ESO La Silla Observatory, Chile; IO:O: 2 m 2 m Liverpool Telescope with IO:O, at the Observatorio del Roque de Los Muchachos, Spain; Las Cumbres Observatory 1m0-03, 1m0-11: node at Siding Spring, Australia; 1m0-04, 1m0-05, 2m0-02: node at Cerro Tololo Inter-American Observatory, Chile; 1m0-10, 1m0-12, 1m0-13: node at South African Astronomical Observatory, South Africa.

(This table is available in its entirety in machine-readable form.)

Table 3
griz Light Curves of DLT16am

Date	JD	Phase (day)	*g*(err) (mag)	*r*(err) (mag)	*i*(err) (mag)	*z*(err) (mag)	Inst
20161116	2457708.60	−4.00	⋯	⋯	>18.7	>18.0	IO:O
20161117	2457709.53	−3.07	⋯	>20.4	>19.9	>19.8	GROND
20161117	2457709.60	−3.00	⋯	⋯	>19.3	>18.4	IO:O
20161118	2457710.53	−2.08	⋯	⋯	>19.3	>18.8	IO:O
20161118	2457711.29	−1.31	>21.7	⋯	⋯	⋯	1m0-10

Note. IO:O: 2 m Liverpool Telescope with IO:O; GROND: MPG/ESO 2.2 m telescope with GROND at the ESO La Silla Observatory, Chile; PROMPT1: 0.41 m PROMPT1 telescope at the Cerro Tololo Inter-American Observatory, Chile; ALFOSC_FASU: 2.56 m Nordic Optical Telescope with ALFOSC_FASU, at the Observatorio del Roque de los Muchachos, Spain; E2V: Las Campanas Observatory 1 m Swope Telescope with the E2V camera, at the Las Campanas Observatory, Chile; Las Cumbres Observatory 1m0-03, 1m0-11: node at Siding Spring, Australia; 1m0-04, 1m0-05, 1m0-09: node at Cerro Tololo Inter-American Observatory, Chile; 1m0-10, 1m0-12, 1m0-13: node at South African Astronomical Observatory, South Africa.

(This table is available in its entirety in machine-readable form.)

Table 4
NIR Light Curves of DLT16am

Date	JD	Phase	*J*(err) (mag)	*H*(err) (mag)	*K*(err) (mag)	Inst
2016115	2457707.77	−4.83	>18.3	>17.7	>16.4	GROND
2016116	2457708.73	−3.87	>19.0	>18.2	>16.7	GROND
2016117	2457709.53	−3.07	>18.4	>17.3	>16.1	GROND
2016119	2457711.78	−0.82	⋯	>15.9	⋯	GROND
2016112	2457714.67	2.07	15.10 (0.29)	14.69 (0.19)	14.05 (0.19)	GROND

Note. GROND: MPG/ESO 2.2 m telescope with GROND, at the ESO La Silla Observatory, Chile. NOTCam: 2.56 m Nordic Optical Telescope with NOTCam, at the Observatorio del Roque de los Muchachos, La Palma, Spain; SOFI: 3.58 m ESO New Technology Telescope with SOFI, at the ESO La Silla Observatory, Chile.

(This table is available in its entirety in machine-readable form.)

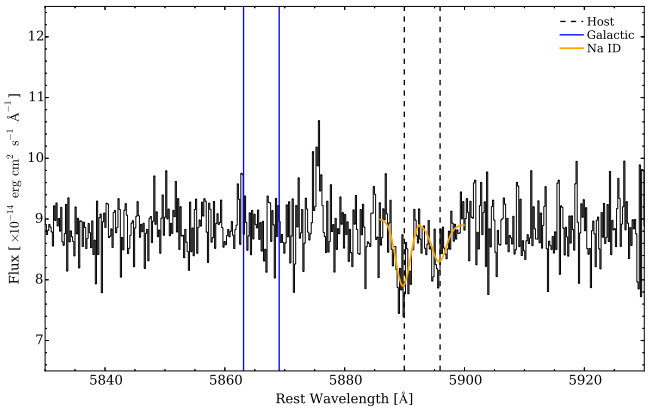

Figure 5. Zoomed-in view of the region of the Na ID doublet in our X-shooter spectrum. The positions of the host and Galactic Na ID lines are marked with black dashed and blue solid lines, respectively. The best-fit Gaussian models for the Galactic Na ID lines are overplotted using orange solid lines.

expansion velocity derived from the spectroscopic analysis, matching the existing luminosity–velocity relation for SNe II.

4.2. Metallicity and Star Formation Rate

After correcting our X-shooter UVB and VIS spectra for the foreground Galactic extinction, redshift (using the values reported above), and host galaxy extinction, we estimated the local metallicity and SFR of NGC 1532 at the position of DLT16am. An identification of the host galaxy lines commonly used in the literature is reported in Figure 7.

Using the calibration of Pilyugin & Mattsson (2011), based on the strong emission lines of O^{++}, N^{+}, and S^{+} (the NS calibration), we estimate a local metallicity of $12 + \log(O/H) = 8.45$ dex or $12 + \log(N/H) = 7.46$ dex, while following Pettini & Pagel (2004) we obtain

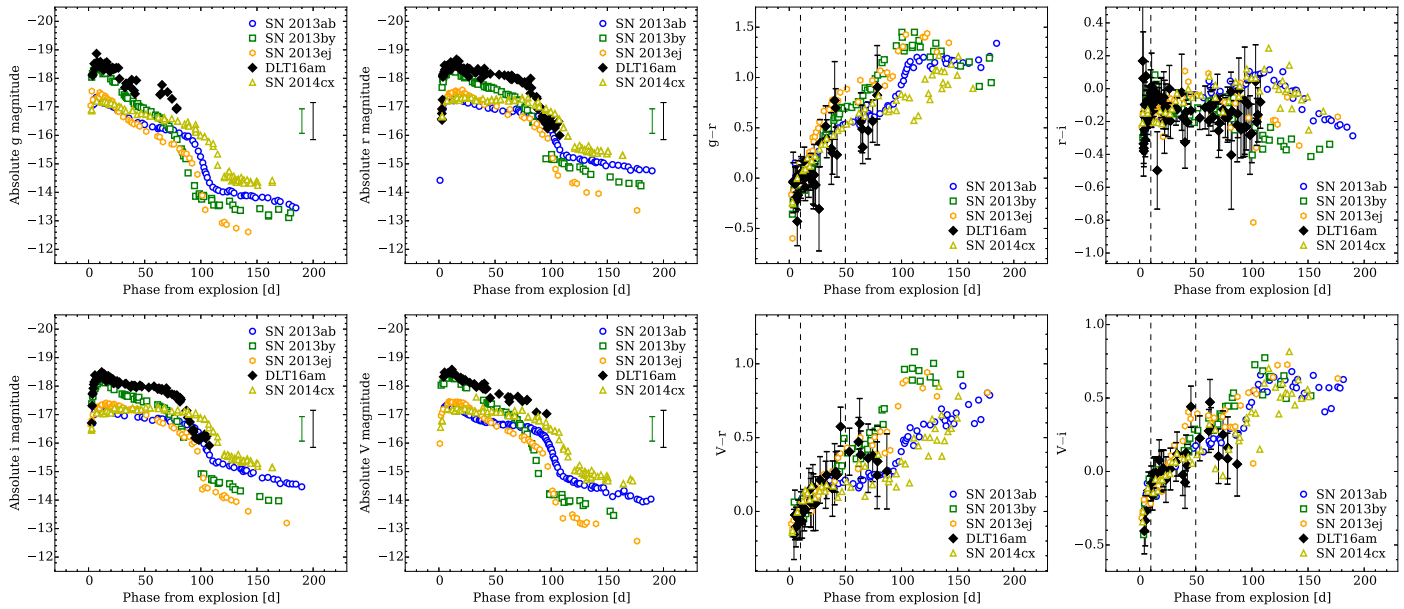

Figure 6. Absolute g-, V-, r-, and i-band light curves (left) and $g-r$, $r-i$, $V-r$, $V-i$ color curves (right) of DLT16am, adopting a contribution of $E(B-V) = 1.95 \pm 0.15$ mag from the host galaxy to the total extinction. The absolute light and color curves of the references adopted to infer the host extinction (see the text for more details) are also shown for comparison. The representative error bar at +200 days and −16 mag in the absolute curve panels corresponds to the uncertainty on the derived extinction in the direction of DLT16am, while the green error bar corresponds to the uncertainty on the distance modulus. The dashed black vertical lines in the color curves delimit the region where the colors of DLT16am were fitted to the references (see the text for additional details).

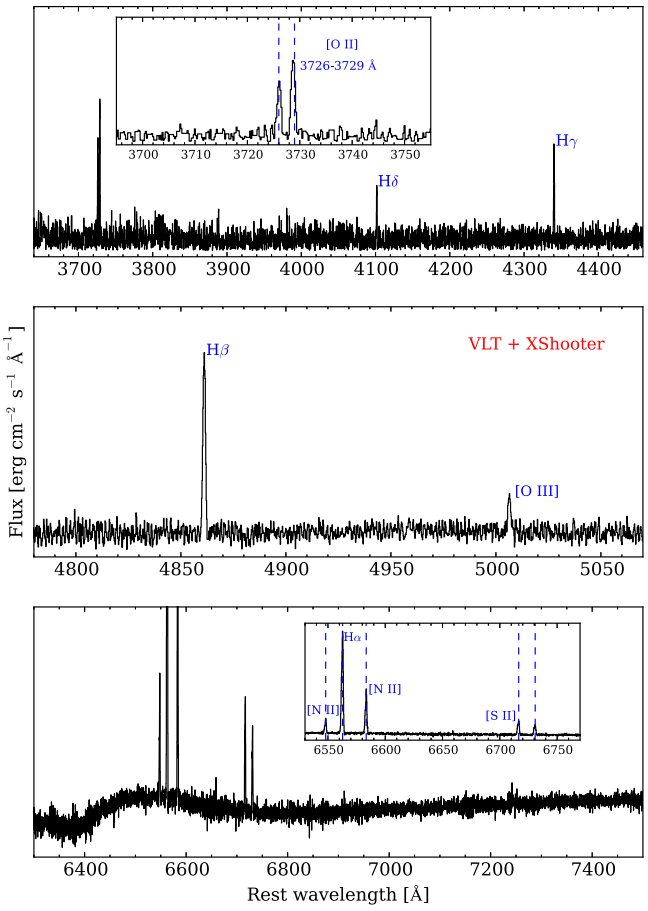

Figure 7. UVB and VIS X-shooter spectra obtained on 2016 December 22. The narrow lines emitted by the host galaxy are identified. The insets in the top and bottom panels show zoomed-in views around the main spectral features.

$12 + \log(\mathrm{O/H}) = 8.67$ and 8.84 dex using the $N2$ indices (Denicoló et al. 2002) and their redefinition of the $O3N2$ (Alloin et al. 1979) indices, respectively. Assuming a solar value of $12 + \log(\mathrm{O/H}) = 8.69$ dex (Asplund et al. 2009), these correspond to $\sim Z_{\odot}$, which is larger than the mean values found by Anderson et al. (2016) for a sample of SNe II, and might be even higher, since metallicity values estimated through line diagnostic are believed to underestimate local abundances (see, e.g., López-Sánchez et al. 2012).

Following Rosa-González et al. (2002), we derive the local SFR from the luminosities of Hα, using the relation given by Kennicutt et al. (1994):

$$\mathrm{SFR(H}\alpha)(M_{\odot}\ \mathrm{yr}^{-1}) = 7.9 \times 10^{-42} L_{\mathrm{H}\alpha}(\mathrm{erg\ s}^{-1}). \quad (1)$$

Accounting for the derived distance of NGC 1532, we obtain a local SFR of $1.64 \times 10^{-1}\ M_{\odot}\ \mathrm{yr}^{-1}$. This is considerably lower than the SFR of NGC 1532, inferred from its far-infrared (FIR) luminosity. The FIR luminosity for NGC 1532 was derived from its 60 μm integrated flux density (9.63 ± 0.034 Jy; Sanders et al. 2003), assuming $L_{\mathrm{FIR}} \simeq 1.7 L_{60\,\mu\mathrm{m}}$ (Chapman et al. 2000) and a distance of 20 Mpc. Using the relation given by Kennicutt (1998),

$$\mathrm{SFR(FIR)}(M_{\odot}\ \mathrm{yr}^{-1}) \simeq 4.5 \times 10^{-44} L_{\mathrm{FIR}}(\mathrm{erg\ s}^{-1}), \quad (2)$$

we obtain a global SFR of $\simeq 2.2\ \mathrm{M}_{\odot}\ \mathrm{yr}^{-1}$, in agreement with the results obtained by Botticella et al. (2012) for the hosts of a sample of nearby ($D < 11$ Mpc) SNe II, corresponding to a specific SFR (sSFR, the SFR per unit of stellar mass) of $\log \mathrm{sSFR} \simeq 10.8$ dex, assuming a stellar mass of $10^{11.14}\ M_{\odot}$ (Muñoz-Mateos et al. 2015).

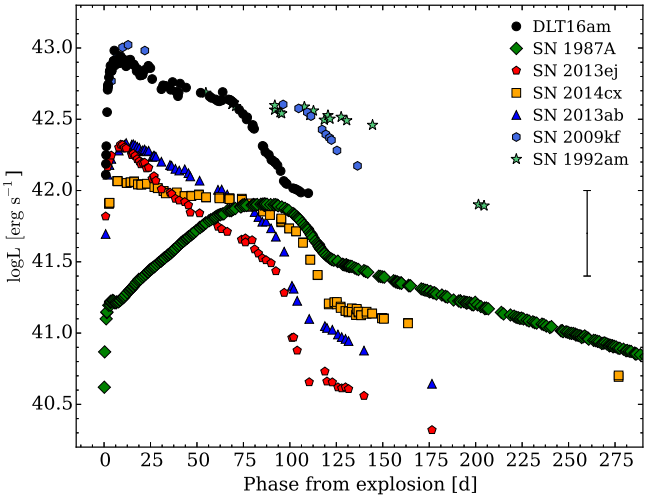

Figure 8. Pseudo-bolometric light curve of DLT16am compared to light curves of other SNe II. The luminosities were obtained using similar filters and integration limits. A representative error bar is also shown, corresponding to the uncertainty on the derived extinction in the direction of DLT16am.

5. Photometry

Roughly 2 weeks before the discovery of DLT16am, the Type Ic SN 2016iae exploded in NGC 1532 (Tonry et al. 2016). Pre-SN images of DLT16am were collected during the photometric follow-up campaign of SN 2016iae carried out with the Las Cumbres Observatory 1 m telescope network, and these images provided the template images used in our photometric analysis. GROND data and NTT acquisition images of SN 2016iae were used as templates for frames obtained with the same instrumental setup.

Prior to the discovery on 2016 November 21.19 UT (Tartaglia et al. 2016b), the last DLT40 non-detection was on 2016 November 19.19 UT ($R > 20.7$ mag), suggesting JD = 2457712.7 ± 1.0 days as the explosion epoch for DLT16am. On the other hand, after the initial discovery, Smith et al. (2016) reported previous detections of the transient on PESSTO V-band acquisition images of SN 2016iae. Although they report a marginal detection on 2016 November 20.10 UT (JD = 2457712.6), when analyzing these archival images we could not find any point source within $\sim 3''$ from the position of DLT16am, while we clearly detected the transient on 2016 November 21.10 UT (JD = 2457713.6). Since the detection limit in the frame obtained on November 20.10 UT is not deep enough to rule out the presence of the transient at this time ($V > 20.2$ mag), we will assume 2457712.6 ± 1.0 days as the explosion epoch, and refer to this date in computing the phases in both our photometric and spectroscopic analysis.

The final apparent light curves are shown in Figure 4, while Figure 6 shows the absolute and color curves obtained after correcting for the host galaxy extinction (see Section 4.1). Due to the high extinction ($E(B-V) = 1.95 \pm 0.15$ mag see Section 4.1), DLT4016am was never detected in the B-band during the first ∼60 days after the explosion, while early detections covering the rise to the light curve maximum at redder wavelengths were available. At early phases, the light curves show relatively fast rises to the maximum in all bands, after which they set on a plateau-like phase with roughly constant magnitudes up to ≃+80 days.

The early evolution ($\lesssim$10 days) of the $g-r$, $r-i$, $V-r$, and $V-i$ colors is fast, suggesting a rapid temperature evolution (see also Section 6), supporting our claim that DLT16am was discovered soon after the explosion.

The pseudo-bolometric light curve of DLT16am was computed converting the available magnitudes to flux densities at the corresponding effective wavelengths, which were subsequently integrated using Simpson's rule. The resulting light curve is shown in Figure 8, along with those of other SNe computed following the same prescriptions and using similar filters. From the analysis of the bolometric light curve of DLT16am, we infer a peak luminosity of $\log L \simeq 43$ dex, which has to be considered a lower limit, since the contribution of the UV flux is, in general, important in early SN light curves. On the other hand, at later times (e.g., on the radioactive-decay tail), UV bands give a minor contribution to the total flux. We can therefore use the pseudo-bolometric light curve to infer the ^{56}Ni mass produced during the SN explosion. This quantity is generally estimated using the method described in Spiro et al. (2014), taking the bolometric luminosity of SN 1987A during the nebular phase as a reference.

We therefore extrapolated the pseudo-bolometric light curve of DLT16am assuming a complete trapping of the γ-rays produced by the ^{56}Co decay (≃1 mag/100 days). Starting from the last observed point (which is likely a few days after the onset of the radioactive tail), we compared the extrapolated luminosity at ≃+150 days with that of SN 1987A computed using the same integration limits and at the same phase, to get a rough estimate of the mass of radioactive ^{56}Ni deposited in the SN ejecta. Using the relation

$$M(^{56}\mathrm{Ni}) = 0.075 M_{\odot} \times L_{\mathrm{SN}}(t)/L_{87A}(t)), \quad (3)$$

we infer a relatively high ^{56}Ni mass of $0.21 \pm 0.09\, M_{\odot}$. A similar amount of radioactive ^{56}Ni was derived for the Type II-P SN 1992am (Schmidt et al. 1994), while a larger limit was given for SN 2009kf ($M_{^{56}\mathrm{Ni}} < 0.4\, M_{\odot}$; see Botticella et al. 2010). Although the derived luminosity might be significantly affected by the large uncertainty on the estimated extinction and distance modulus, we remark that the photospheric expansion velocity inferred from the spectroscopic analysis is in agreement with the derived bright absolute i-band magnitude (and hence the derived total reddening) for DLT16am, according to the existing luminosity–velocity relation (Hamuy & Pinto 2002) for SNe II (see Section 7). In addition, the derived ^{56}Ni also mass seems to be in agreement with the trend followed by SNe II, with comparable photospheric velocities and absolute magnitudes (see Hamuy 2003a).

6. Spectroscopy

Our spectroscopic follow-up campaign started on 2016 November 22.64 UT (≃2 days after the explosion), lasting up to 2017 March, 7.01 UT (at ≃110 days). NIR spectra were obtained within the same period, with a lower cadence. The flux calibration was checked using photometric information obtained during the closest nights, scaled using low-order polynomials.

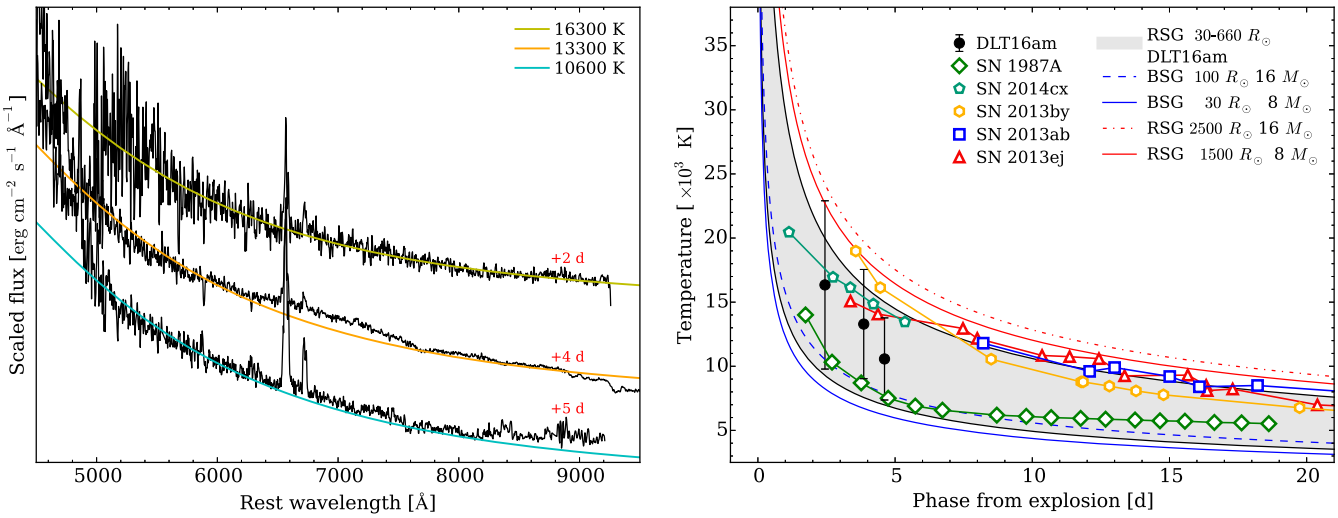

Figure 9. Left: blackbody fits to the early spectra of DLT16am. The spectra have been corrected for the derived total extinction in the direction of DLT16am. Right: progenitor radius of DLT16am constrained using the formalism of Rabinak & Waxman (2011). Models for RSGs and BSGs (red and blue lines, respectively) are also shown, while the range of radii obtained for DLT16am is delimited by black lines. Temperature evolutions obtained for other SNe II are also shown for comparison.

6.1. Optical Spectra

Early spectra are dominated by a nearly featureless and very red continuum (before reddening correction), with narrow Hα and [S II] lines from the host and little or no flux at wavelengths shorter than 5000 Å. After correcting for the foreground Galactic extinction ($A_V = 0.042$ mag), redshift ($z = 0.00456$, inferred from the X-shooter spectrum; see Section 4) and host extinction ($A_V \simeq 6.12$ mag), we estimated the temperature of the ejecta at early phases using a blackbody function to fit the spectral continuum through the CURVE_FIT tool available in the SciPy[41] package (Jones et al. 2001; Van Der Walt et al. 2011). We find a rapid decrease, from 16300 ± 6600 K at +2 days to 10600 ± 3200 K at +5 days, in agreement with the fast color evolution within the early phases (see Section 5), although the large uncertainties might suggest a lack of clear evolution in temperature. The errors on the derived temperatures were estimated by applying different extinction values, within the range of the derived uncertainty on the reddening (see Section 4.1). At later phases ($t > +5$ days), we could not determine the temperatures, since no contribution from the SN to the spectral continuum at $\lambda < 6000$ Å was observed, due to the high extinction (see Section 4.1) and the low signal-to-noise ratio (S/N) of later spectra.

Figure 9 (left panel) shows the results of the blackbody fit to the spectra up to $\simeq$+5 days. As discussed by Rabinak & Waxman (2011), the timescale of the cooling phase subsequent to the SN shock breakout heating of the progenitor envelope strongly depends on the initial progenitor properties, such as its radius, density profile, opacity, and composition. Using their formalism (i.e., their Equation (12)), we infer a rough estimate of the progenitor radius fitting the temperature evolution of DLT16am during the first $\simeq$5 days of its spectroscopic evolution (see Rabinak & Waxman 2011 and Rubin & Gal-Yam 2017, for an analysis on the limitations of analytic models). Figure 9 (right panel) shows the resulting fit (obtained assuming an explosion energy of 10^{51} erg and a typical optical opacity for a H-rich gas, $\kappa = 0.34$ cm^2 g^{-1}; Rabinak & Waxman 2011), along with the temperature evolution obtained for other SNe II.

Direct imaging in deep pre-SN archival images confirmed the claim that the majority of SNe II have red super-giant (RSG) progenitors (see, e.g., Maund et al. 2005; Smartt 2009; Fraser et al. 2011; Van Dyk et al. 2012a, 2012b). We therefore adopt the typical mass range for RSG progenitors (8–17 $M_\odot$; Smartt 2009), and using the Rabinak & Waxman (2011) formalism we obtain a radius of 30–660 $R_\odot$ for the progenitor of DLT16am, where the uncertainty is largely due to the error on the estimated reddening. Although the model is weakly dependent on the mass of the progenitor (see Rabinak & Waxman 2011), the large uncertainty on the derived temperatures does not allow us to rule out a blue super-giant (BSG) star as a viable progenitor for DLT16am (see Figure 9, right panel).

From +24 days a broad FWHM (FWHM $\simeq$ 9000 km s^{-1}) Hα feature in emission starts to dominate the flux, masking the presence of the host [S II] lines, with blueshifted peaks typical of SNe II (see Anderson et al. 2014a, for a discussion). Following Anderson et al. (2014a) and Gutiérrez et al. (2014), we measure the Hα blueshifted emission offset and the ratio between the EWs of its absorption and emission P-Cygni components (a/e). We find a significant blueshifted Hα peak ($V \simeq 3300$ km s^{-1}) at +30 days and a small contribution of the absorption component to the Hα P-Cygni profile ($a/e \simeq 0.06$), both indicative of fast-declining light curves during the plateau phase and in agreement with the results of our photometric analysis (see Section 7). From the same phase we also detect the NIR (8498, 8542, 8662 Å) Ca II and O I (7772, 7774, 7775 Å) triplets, both becoming more evident at later phases. C I λ9095 and Mg II λ9218 lines appear between +58 and +59 days, while forbidden [Ca II] lines are visible from +91 days, marking the onset of the nebular phase, possibly blended with the [O II] 7319, 7330 Å doublet. From the same phase we note a significant change in the relative strengths of the Ca II NIR triplet, which is likely caused by the appearance of the nebular [O I] 8446 Å line.

[41] https://www.scipy.org/

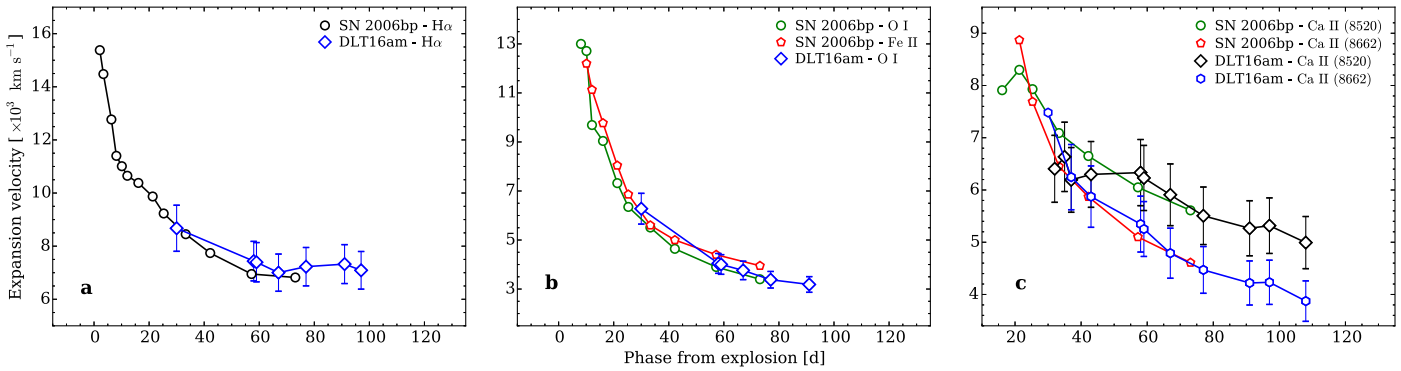

Figure 10. Expansion velocity evolutions derived from Hα (a), O I λ7773 and Fe II λ5169 (b) and the NIR Ca II triplet (c), compared to those derived for SN 2006bp. The comparison is made on the basis of the best match of the DLT16am +59 days spectrum obtained with the SNID tool.

From the positions of the minima of the P-Cygni absorption profiles, we derived an estimate of the expansion velocities for different ions. Hα P-Cygni profiles are clearly visible only from +30 days, when we derive an expansion velocity of ≃8700 km s^{-1}, slowly declining to ≃7100 km s^{-1} at +97 days (see also Figure 10, panel a). While the Fe II λ5169 line is generally assumed as a good tracer of the photospheric velocity, we could not detect this line in any of our spectra of DLT16am due to the high extinction (see Section 4.1). We therefore obtained a rough estimate of the photospheric velocity from the minima of the prominent O I triplet, getting a relatively fast evolution from ≃6300 km s^{-1} (at +30 days) to ≃3000 km s^{-1} (at +97 days; see Section 7 and Figure 10 for a detailed discussion). The Ca II NIR triplet was partially resolved, and we inferred an expansion velocity declining from ≃6400 km s^{-1} to 5000≃ km s^{-1} for the blend of the 8498, 8542 Å lines, and from 7500 to 3900 km s^{-1} for the 8662 Å line.

6.2. Near Infrared Spectra

At +7 days, our SOFI spectrum shows an almost featureless continuum, while at later phases spectra show a significant metamorphosis, as broad H lines with prominent P-Cygni profiles start to dominate the flux. Following the NIR line identifications proposed for SNe 2004et (Maguire et al. 2010) and 1998S (Pozzo et al. 2004), we identify most of the main H Paschen (from Paα up to Paζ) and Brackett (from Brγ up to Brη) lines, although the Paγ line is most likely a blend with He I (10830 Å). Beginning on +34 days, we also detect the Ca II NIR triplet. We also identify Sr II λ10327 in the blue part of the spectra beginning on +43 days, when the feature is still partially blended with the Paδline, becoming more evident at later phases.

C I and Mg II lines appear from +54 days, in agreement with the analysis performed on the optical spectra (although we cannot rule out the presence of these lines also at +43 days). From the Paβ absorption minima, we infer an expansion velocity decreasing from ≃8340 km s^{-1} at +34 days to ≃3460 km s^{-1} at +107 days, which is consistent with the evolution derived from Hα (see above); while measuring the prominent blue minimum in the blue part of the Paγ+He I 10830 Å profile, we infer higher expansion velocities, declining from ≃9000 km s^{-1} to ≃5660 km s^{-1} from +34 days to +107 days, respectively.

From +43 days we notice a second absorption feature in the blue part of the P-Cygni absorption component of Paβ,

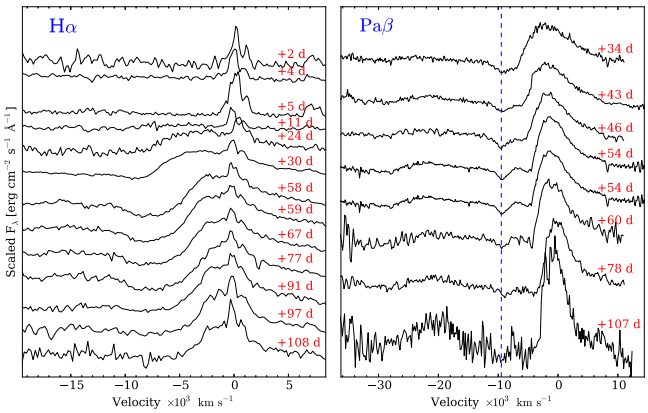

Figure 11. Details of the evolution of the Hα and Paβ profiles of DLT16am in the velocity space. The position of the blue absorption feature in the Paβ profile, with a constant expansion velocity of 9400–9500 km s^{-1} is marked with a dashed blue line. Phases refer to the epoch of the explosion. Spectra with lower S/Ns are not included.

becoming more evident at later phases, which might be attributed to a rapidly expanding outer H shell moving at a roughly constant velocity (9400–9500 km s^{-1}). High-velocity (HV) components not evolving in time were observed also in the Hα profile and He I 10830 Å of other SNe II (see, e.g., the case of SNe 2009bw; Inserra et al. 2012, 1999em and 2004dj; Chakraborti et al. 2012 and the discussion in Chugai et al. 2007) and attributed to weak interaction between the SN ejecta and a pre-existing CSM surrounding the progenitor star. Analyzing HV components in the Hα and He I 10830 Å profiles during the photospheric phase, Chugai et al. (2007) computed a model for ejecta–circumstellar interaction in SNe II-P. Although the expansion velocities inferred from the Paγ P-Cygni minimum suggest that the entire absorption component might be mainly attributed to the He I 10830 Å line, Figure 11 shows that a similar feature was never observed in the Hα profile at any phase, with the possible exception of the +58 days spectrum. On the other hand, the S/N of our spectra is not sufficient to safely rule out the presence of this feature at optical wavelengths.

7. Comparison with Other SNe II

In Figure 6 wecompared the main photometric properties of a sample of luminous and more canonical SNe II. The left panels show that DLT16am is brighter than the normal Type II SNe 2014cx (Huang et al. 2016) and 2013ej (Valenti

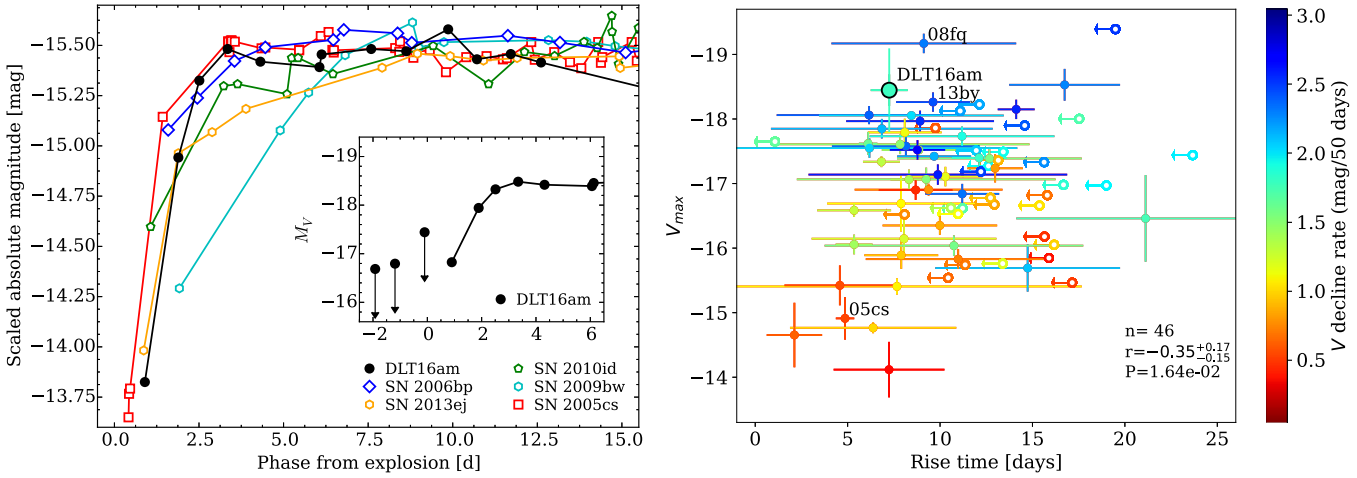

Figure 12. Left: early absolute V-band light curve of DLT16am compared to other SNe II (the r-band light curve of SN 2010id is shown for comparison). The light curves are scaled to the plateau luminosity of SN 2010id. The phases refer to the epochs of the explosions. Right: V-band absolute magnitude vs. rise time for the same sample of SNe II, color-coded according to their V-band decline rate (S_{50V}). n is the number of transients in the plot, r is the Pearson s-correlation coefficient, and P is the probability of detecting a correlation by chance, as in Valenti et al. (2016).

et al. 2014, although the large uncertainties on the extinction suggest comparable plateau magnitudes), while high luminosities are not unusual among SNe II (see, e.g., the case of SN 2013by; Valenti et al. 2015).

Following the prescriptions of Valenti et al. (2016), we estimate photometric parameters using the V-band photometric evolution. As the V-band maximum we consider the point at which the variation in magnitude is less than 0.1 mag day^{-1}, while S_{50V}, the decline rate in mag/50 days, was computed soon after the maximum (10 days after the explosion) to +50 days after the explosion. Figure 12 summarizes the results of this analysis, compared to those obtained for other SNe II (Valenti et al. 2016). The V-band maximum for DLT16am occurs on JD = 2457719.95, corresponding to an absolute magnitude $M_V = -18.48 \pm 0.77$ mag (where the error is almost entirely due to the uncertainty on the reddening and the distance modulus) and to a relatively fast rise time of 7.4 ± 1.0 days. At redder wavelengths we find longer rises (10.9, 11.4, and 11.9 days in the r-, i-, and z-bands, respectively), in agreement with the results obtained by González-Gaitán et al. (2015) on a large sample of SNe II. In the r-band, on the other hand, we find that DLT16am has a relatively slow rise if compared to the sample of Rubin et al. (2016)

Comparing the early-time absolute r-band light curve of SN 2010id with those of SNe 2005cs (Pastorello et al. 2009) and SN 2006bp (Quimby et al. 2007), Gal-Yam et al. (2011) suggested a possible trend for subluminous and "normal" events, with faster rises with a sharp onset of the flat plateau for fainter objects, with SN 2006bp showing a more gradual transition over a longer period. Including the slow-rising SNe 2009bw (Inserra et al. 2012) and 2013ej R-band light curves in the comparison, Valenti et al. (2014) also argued that slow-rising SNe II might be brighter than fast-rising transients. The fast rise and the bright absolute magnitude shown by DLT16am seem to contradict these predictions, confirming the results obtained by Rubin et al. (2016) on a sample of R-band light curves of SNe II. In Figure 12, left panel, we compare the early V-band absolute light curve of DLT16am with those of a sample of subluminous

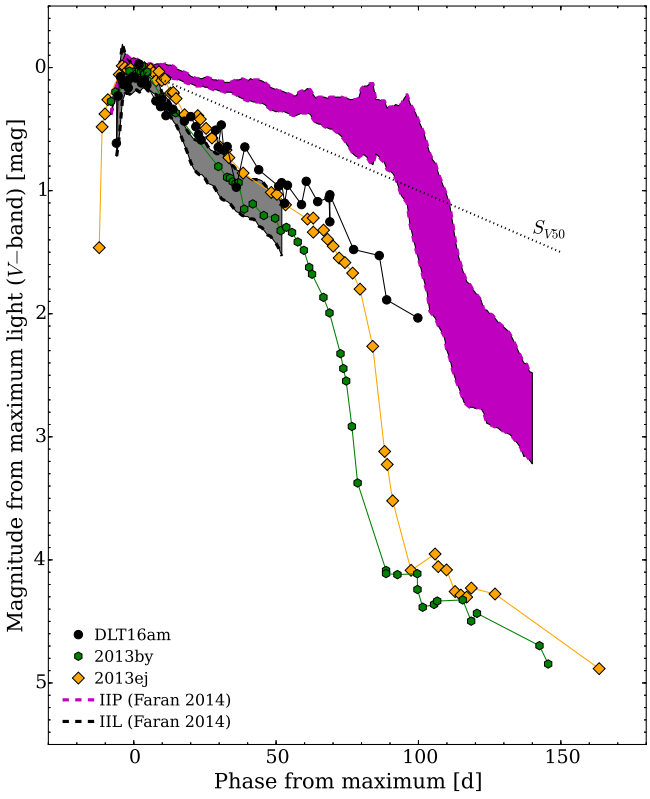

Figure 13. Absolute V-band light curve of DLT16am and other similar transients compared with templates computed by Faran et al. (2014a, 2014b) for SNe II. The dotted black line marks the limiting slope (S_{50V}; see the text for details) between Type II-P (magenta dashed lines) and II-L (black dashed models) SNe.

(SNe 2005cs; Pastorello et al. 2009 and 2010id; Gal-Yam et al. 2011), normal (SNe 2006bp; Quimby et al. 2007 and 2013ej Valenti et al. 2014), and luminous (SN 2013by; Valenti et al. 2015 and DLT16am) SNe II, all scaled to the luminosity of the plateau of SN 2010id, in order to gain better insight into their different rise times. We find a particularly good match with the subluminous SN 2005cs,

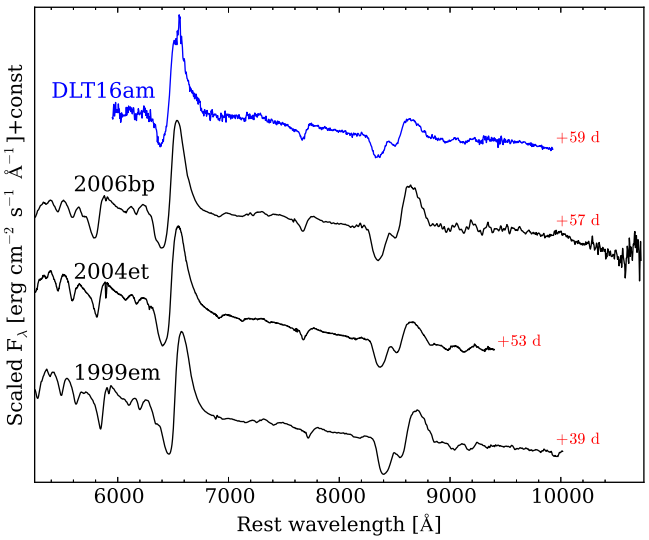

Figure 14. Comparison of the +59 days spectrum of DLT16am with those of a sample of SNe II at similar phases. Comparison objects were selected on the basis of the results obtained using the SNID comparison tool (Blondin & Tonry 2007). Fluxes have been scaled to arbitrary constants.

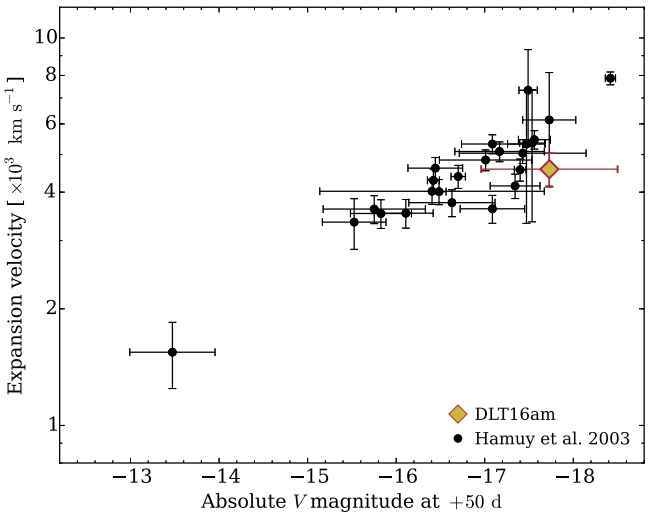

Figure 15. Expansion velocity (inferred from Fe II λ5169 absorption minima) vs. V-band absolute magnitude for a sample of SNe II. Velocities and luminosities have been computed 50 days after the explosion (roughly the midpoint of the plateau phase; see Hamuy et al. 2001). DLT16am is marked with a yellow and red diamond.

while more luminous transients, like SNe 2006bp and 2013ej, seem to have significantly longer rises to maximum light. This trend is confirmed by the comparison with a larger sample of SNe II shown in Figure 12 (right panel). DLT16am lies close to the brighter end of the absolute peak magnitude range, with a rise time comparable to those displayed by the faintest objects. Comparing the r-band absolute peak magnitude and rise time to the sample of Rubin et al. (2016; see their Figure 10), on the other hand, we find a longer rise time, while DLT16am falls in a scarcely populated region of their luminosity-rise time diagram. On the other hand, we have to remark that this might be due to the lack of transients with well constrained explosion epochs (see, e.g., the case of SN 2008fq and the large uncertainties in the rise times of the brightest objects).

The historical classification of Type II in II-P and II-L SNe has recently been debated (see, e.g., Arcavi et al. 2012; Anderson et al. 2014b; Faran et al. 2014a, 2014b; Sanders et al. 2015; Valenti et al. 2016). In order to give an accurate classification of DLT16am, in Figure 13 we compare the V-band light curve of DLT16am to the Type II-P and II-L SNe templates computed by Faran et al. (2014b, 2014a). Although DLT16am shows photometric features typically observed in SNe II-P (namely an extended plateau after maximum, with a subsequent steep drop in magnitude around +80 days), like SN 2013by (Valenti et al. 2014) its V-band light curve lies close to the bright end of the II-L templates, in an intermediate region between II-L and II-P templates. This is in agreement with the decline rate derived from the V-band light curve ($S_{50V} = 0.84 \pm 0.04$ mag/50 days), which, according to Faran et al. (2014a), is greater than the limit for SNe II-P (0.5 mag/50 days; see Figure 13). Following Rubin & Gal-Yam (2016) and their proposed classification based on the early light curves morphology, we compare the r-band light curve of DLT16am to the results of their analysis on the sample of Rubin et al. (2016), obtaining a good match with their fast rise–fast decline (II-FF) cluster of SNe II.

Figure 14 shows a comparison of our +59 days spectrum with those of other SNe II, based on the best fits of the spectral features to archival spectra obtained using the "Supernova Identification" (SNID[42]; Blondin & Tonry 2007)) tool. While the best match was obtained with the Type II-P SN 2006bp (Quimby et al. 2007; Dessart et al. 2008), good fits of the spectral features were also obtained with the Type II-P SNe 2004et (Sahu et al. 2006; Misra et al. 2007; Maguire et al. 2010) and 1999em (Hamuy et al. 2001; Leonard et al. 2002; Elmhamdi et al. 2003; Dessart & Hillier 2006). Based on this similarity, we compared the expansion velocities of DLT16am with those obtained for SN 2006bp, obtaining similar values for all the ions visible in both sets of spectra (see Figure 10). Due to the high extinction, we could not compare the expansion velocities inferred from Fe II (5169 Å) or Sc II (6246 Å), which are typically considered good indicators of the photospheric velocity. On the other hand, SN 2006bp shows similar Fe II (5169 Å) and O I (7773 Å) expansion velocities (see Figure 10, panel b) and based on the strong spectroscopic similarities between the two transients, we can therefore use the velocity evolution inferred from the O I minima as a rough estimate of the photospheric expansion velocity for DLT16am. Using the existing luminosity–velocity relation for SNe II (Hamuy & Pinto 2002; Hamuy 2003b), we can therefore perform an independent consistency check on the derived host galaxy reddening in the direction of DLT16am (see Section 4.1). Hamuy & Pinto (2002) used +50 days as an indicative epoch (roughly the midpoint of the plateau phase), and although DLT16am shows a relatively short plateau lasting ≃80 days, we will adopt the same approach, comparing the expansion velocity and absolute V-magnitude with those obtained from the sample of Hamuy (2003b) at similar phases. A similar approach was also adopted for the absolute V-band luminosity, where we took the uncertainty on the distance modulus and the total extinction as an estimate of the error on the derived magnitude. In Figure 15 we compare the results for DLT16am with those obtained for the sample of Hamuy (2003b). With a photospheric velocity of ≃4585 km s^{-1}

[42] https://people.lam.fr/blondin.stephane/software/snid/

and an absolute V-band magnitude at $+50$ days of $M_V = -17.73 \pm 0.77$ mag, DLT16am falls in the region of other luminous SNe II, in agreement with the expectation that luminous transients have higher expansion velocities (see also Rubin et al. 2016). The correlation between absolute peak magnitudes and expansion velocity was recently confirmed by Gutiérrez et al. (2017), who also confirmed the previous claim of Anderson et al. (2014a) and Valenti et al. (2016) that brighter SNe II show shorter plateau phases and steeper decline rates. Similar results were also reported by Galbany et al. (2016) by analyzing the light curves of a large sample of SNe II.

8. Summary and Conclusions

We have discussed the results of our analysis of the photometric and spectroscopic data obtained during our follow-up campaign of the Type II SN DLT16am (also known as SN 2016ija). The transient was discovered during the ongoing DLT40 survey, which is monitoring a sample of galaxies in the nearby universe in search of young SNe within the first days after explosion.

Early spectra showed a highly reddened, nearly featureless continuum, while H, Ca II, and O I lines with prominent P-Cygni profiles gradually appear at later phases. A comparison of the colors of DLT16am with those of other similar transients during the plateau phase suggests a contribution of $E(B - V) = 1.95 \pm 0.15$ mag from the host galaxy (NGC 1532) to the total extinction (see Section 4.1 and Figure 6). Although DLT16am was clearly detected by our survey at redder optical wavelengths, its substantial extinction of $Av \simeq 6$ mag supports the claim that optical surveys might be missing a significant fraction of nearby, highly reddened SNe (e.g., Mattila et al. 2012; Jencson et al. 2017). Other examples of recent heavily obscured CCSNe observed in nearby galaxies include SN 2009hd (Elias-Rosa et al. 2011), SN 2005at (Kankare et al. 2014a), and SN 2013fc (Kangas et al. 2016), SPIRITS15c and SPIRITS14buu; Jencson et al. 2017, or SNe 2008cs, 2011hi, and 2010P Kankare et al. 2008, 2012, 2014b). Such events can have important implications for a comparison between CCSN rates andcosmic star formation history.

Assuming a standard ($R_V = 3.1$) extinction law (Cardelli et al. 1989) and a distance modulus $\mu = 31.51 \pm 0.43$ mag (Tully et al. 2013), we obtain a relatively bright absolute peak magnitude ($M_V = -18.48 \pm 0.77$ mag) compared to those displayed by other Type II-P-like SNe.

The absolute magnitude at $+50$ days is consistent with the photospheric velocity inferred at the same phase, according to the existing luminosity–velocity relation for SNe II (see Hamuy & Pinto 2002; Hamuy 2003b, and Figure 15). The derived slope within 50 days from the explosion (S_{50V}; see Section 7) suggests a relatively steep decline during the plateau phase ($S_{50V} = 0.84 \pm 0.04$ mag/50 days), which, according to Faran et al. (2014a; who gave a limit of 0.5 mag/50 days to the maximum slope for SNe II-P), means that DLT16am should be considered an SN II-L. A similar conclusion was reached by Valenti et al. (2014) in their analysis of SN 2013by, which, like DLT16am, showed an extended plateau, with a drop in magnitude around 80 days after the explosion (see also Figure 6).

In Figure 12 we have shown a comparison of the fundamental photometric parameters inferred for DLT16am with those obtained for a sample of SNe II. The fast rise time (7.4 ± 1.0 days) and the bright V-band absolute magnitude at maximum ($M_V = -18.48 \pm 0.77$ mag) seem to contradict the prediction that luminous SNe II have long rise times compared to those of subluminous events. The lack of other SNe II in the region where DLT16am falls highlights its peculiarity, but might also be due to the lack of transients with well constrained explosion epochs.

It is therefore crucial to increase our sample of SNe II with well constrained explosion epochs and rise times, providing early discoveries and subsequent multi-wavelength data. With its estimated rate of $\simeq$4–5 SNe II per year discovered within 1 day from the explosion, confirmed by the number of discoveries during the first year of operations, the DLT40 survey will significantly increase the number of early discoveries, helping to further explore correlations between fundamental parameters of SNe II.

This work is based on observations collected at: the Very Large Telescope operated by the European Organisation for Astronomical Research in the Southern hemisphere, Chile as part of the ESO large programme 198.A-0915; ESOO La Silla Observatory as part of PESSTO (197.D-1075.191.D-0935); the Gemini Observatory, under program GN-2016B-Q-57, which is operated by the Association of Universities for Research in Astronomy, Inc., under a cooperative agreement with the NSF on behalf of the Gemini partnership: the National Science Foundation (United States), the National Research Council (Canada), CONICYT (Chile), Ministerio de Ciencia, Tecnología e Innovación Productiva (Argentina), and Ministério da Ciência, Tecnologia e Inovação (Brazil).

This work is based on observations made with the Nordic Optical Telescope, operated by the Nordic Optical Telescope Scientific Association at the Observatorio del Roque de los Muchachos, La Palma, Spain, of the Instituto de Astrofisica de Canarias.

This paper includes data gathered with the 6.5 m *Magellan* Telescopes located at Las Campanas Observatory, Chile.

This work makes use of observations from the Las Cumbres Observatory network of telescopes.

This work includes data obtained with the Swope Telescope at Las Campanas Observatory, Chile, as part of the Swope Time Domain Key Project (PI Piro, Co-PIs Shappee, Drout, Madore, Phillips, Foley, and Hsiao).

SNOoPy is a package for SN photometry using PSF-fitting and/or template subtraction developed by E. Cappellaro. A package description can be found at http://sngroup.oapd.inaf.it/snoopy.html.

FOSCGUI is a graphic user interface aimed at extracting SN spectroscopy and photometry obtained with FOSC-like instruments. It was developed by E. Cappellaro. A package description can be found at http://sngroup.oapd.inaf.it/foscgui.html.

Research by D.J.S. and L.T.L. is supported by NSF grants AST-1412504 and AST-1517649.

C.G. acknowledges support from the Carlsberg Foundation.

R.C. and M.S. acknowledge support from STFC grant ST/L000679/1 and EU/FP7-ERC grant No. 615929. T.W.C. acknowledges the support through the Sofia Kovalevskaja Award to P. Schady from the Alexander von Humboldt Foundation of Germany.

Part of the funding for GROND (both hardware as well as personnel) was generously granted from the Leibniz-Prize to Prof. G. Hasinger (DFG grant HA 1850/28-1).

Support for G.P. is provided by the Ministry of Economy, Development, and Tourism's Millennium Science Initiative through grant IC120009, awarded to The Millennium Institute of Astrophysics, MAS.

J.H. acknowledges financial support from the Finnish Cultural Foundation and the Vilho, Yrjö, and Kalle Väisälä Foundation of the Finnish Academy of Science and Letters.

D.A.H., C.M., and G.H. are supported by NSF grant 1313484.

M.D.S. acknowledges support by a research grant (13261) from the VILLUM FONDEN and for financial support of NUTS by the Instrument Center for Danish Astrophysics (IDA).

L.G. was supported in part by the US National Science Foundation under grant AST-1311862.

M.M.P., N.M., and E.Y.H. acknowledge the support provided by the National Science Foundation under grant No. AST-1008343, AST-1613472, and AST-1613426.

A.G.-Y. is supported by the EU via ERC grant No. 725161, the Quantum Universe I-Core program, the ISF, the BSF Transformative program and by a Kimmel award.

K.M. acknowledges support from the STFC through an Ernest Rutherford Fellowship.

The UCSC group is supported in part by NSF grant AST-1518052, the Gordon & Betty Moore Foundation, and from fellowships from the Alfred P. Sloan Foundation and the David and Lucile Packard Foundation to R.J.F.

Facilities: VLT:Kueyen (X-shooter spectrograph Vernet et al. 2011), NTT (EFOSC2 Buzzoni et al. 1984 and SOFI Moorwood et al. 1998 spectrographs), Gemini:Gillett (GNIRS spectrograph; Elias et al. 2006), NOT (ALFOSC and NOTCam cameras), Magellan:Baade (FIRE spectrograph), FTN, FTS (FLOYDS spectrographs), LCOGT, Swope, Liverpool:2m (IO:O camera), Max Planck:2.2m (GROND camera), CTIO:PROMPT (PROPT5 telescope; Reichart et al. 2005).

Software: SNID (Blondin & Tonry 2007), FOSCGUI (http://graspa.oapd.inaf.it/foscgui.html), SNOOPY (http://sngroup.oapd.inaf.it/snoopy.html), PYSALT (Crawford et al. 2010), XDGNIRS, firehose (Simcoe et al. 2013). ESOREFLEX (Freudling et al. 2013), SCIPY (https://www.scipy.org/), PYRAF, IDL, HOTPANTS (Becker 2015).

ORCID iDs

L. Tartaglia https://orcid.org/0000-0003-3433-1492
S. Valenti https://orcid.org/0000-0001-8818-0795
I. Arcavi https://orcid.org/0000-0001-7090-4898
T.-W. Chen https://orcid.org/0000-0003-1532-0149
A. Cikota https://orcid.org/0000-0001-7101-9831
D. Coulter https://orcid.org/0000-0003-4263-2228
M. Della Valle https://orcid.org/0000-0003-3142-5020
A. Gal-Yam https://orcid.org/0000-0002-3653-5598
G. Hosseinzadeh https://orcid.org/0000-0002-0832-2974
D. A. Howell https://orcid.org/0000-0003-4253-656X
E. Y. Hsiao https://orcid.org/0000-0003-1039-2928
C. Inserra https://orcid.org/0000-0002-3968-4409
H. Kuncarayakti https://orcid.org/0000-0002-1132-1366
P. A. Mazzali https://orcid.org/0000-0001-6876-8284
C. McCully https://orcid.org/0000-0001-5807-7893
M. M. Phillips https://orcid.org/0000-0003-2734-0796
G. Pignata https://orcid.org/0000-0003-0006-0188
D. E. Reichart https://orcid.org/0000-0002-5060-3673
J. Sollerman https://orcid.org/0000-0003-1546-6615
M. Sullivan https://orcid.org/0000-0001-9053-4820

References

Alloin, D., Collin-Souffrin, S., Joly, M., & Vigroux, L. 1979, A&A, 78, 200
Anderson, J. P., Dessart, L., Gutierrez, C. P., et al. 2014a, MNRAS, 441, 671
Anderson, J. P., González-Gaitán, S., Hamuy, M., et al. 2014b, ApJ, 786, 67
Anderson, J. P., Gutiérrez, C. P., Dessart, L., et al. 2016, A&A, 589, A110
Arcavi, I., Gal-Yam, A., Cenko, S. B., et al. 2012, ApJL, 756, L30
Arcavi, I., Hosseinzadeh, G., Brown, P. J., et al. 2017, ApJL, 837, L2
Asplund, M., Grevesse, N., Sauval, A. J., & Scott, P. 2009, ARA&A, 47, 481
Barbarino, C., Botticella, M. T., Dall'Ora, M., et al. 2017, MNRAS, 471, 2463
Becker, A. 2015, HOTPANTS: High Order Transform of PSF ANd Template Subtraction, Astrophysics Source Code Library, ascl:1504.004
Bellm, E. 2014, in The Third Hot-wiring the Transient Universe Workshop, ed. P. R. Wozniak et al., 27
Bersten, M. C., Benvenuto, O. G., Nomoto, K., et al. 2012, ApJ, 757, 31
Bloemen, S., Groot, P., Nelemans, G., & Klein-Wolt, M. 2015, in ASP Conf. Ser. 496, Living Together: Planets, Host Stars and Binaries, ed. S. M. Rucinski, G. Torres, & M. Zejda (San Francisco, CA: ASP), 254
Blondin, S., & Tonry, J. L. 2007, ApJ, 666, 1024
Bloom, J. S., Kasen, D., Shen, K. J., et al. 2012, ApJL, 744, L17
Bose, S., Valenti, S., Misra, K., et al. 2015, MNRAS, 450, 2373
Botticella, M. T., Smartt, S. J., Kennicutt, R. C., et al. 2012, A&A, 537, A132
Botticella, M. T., Trundle, C., Pastorello, A., et al. 2010, ApJL, 717, L52
Bowen, I. S., & Vaughan, A. H., Jr. 1973, ApOpt, 12, 1430
Brown, T. M., Baliber, N., Bianco, F. B., et al. 2013, PASP, 125, 1031
Buzzoni, B., Delabre, B., Dekker, H., et al. 1984, Msngr, 38, 9
Calzetti, D., Armus, L., Bohlin, R. C., et al. 2000, ApJ, 533, 682
Cao, Y., Kulkarni, S. R., Howell, D. A., et al. 2015, Natur, 521, 328
Cappellaro, E., Botticella, M. T., Pignata, G., et al. 2015, A&A, 584, A62
Cardelli, J. A., Clayton, G. C., & Mathis, J. S. 1989, ApJ, 345, 245
Chakraborti, S., Yadav, N., Ray, A., et al. 2012, ApJ, 761, 100
Chambers, K. C., Magnier, E. A., Metcalfe, N., et al. 2016, arXiv:1612.05560
Chapman, S. C., Scott, D., Steidel, C. C., et al. 2000, MNRAS, 319, 318
Chen, T.-W., Schady, P., & Kruehler, T. 2016, ATel, 9789
Chugai, N. N., Chevalier, R. A., & Utrobin, V. P. 2007, ApJ, 662, 1136
Crawford, S. M., Still, M., Schellart, P., et al. 2010, Proc. SPIE, 7737, 773725
Dahlen, T., Strolger, L.-G., Riess, A. G., et al. 2012, ApJ, 757, 70
de Vaucouleurs, G., de Vaucouleurs, A., Corwin, H. G., Jr., et al. 1991, Third Reference Catalogue of Bright Galaxies. Vol. I, Vol. II, Vol. III (New York: Springer)
Dessart, L., Blondin, S., Brown, P. J., et al. 2008, ApJ, 675, 644
Dessart, L., & Hillier, D. J. 2006, A&A, 447, 691
Denicoló, G., Terlevich, R., & Terlevich, E. 2002, RMxAC, 12, 257
Elias, J. H., Joyce, R. R., Liang, M., et al. 2006, Proc. SPIE, 6269, 62694C
Elias-Rosa, N., Benetti, S., Turatto, M., et al. 2008, MNRAS, 384, 107
Elias-Rosa, N., Van Dyk, S. D., Li, W., et al. 2011, ApJ, 742, 6
Elmhamdi, A., Danziger, I. J., Chugai, N., et al. 2003, MNRAS, 338, 939
Faran, T., Poznanski, D., Filippenko, A. V., et al. 2014a, MNRAS, 445, 554
Faran, T., Poznanski, D., Filippenko, A. V., et al. 2014b, MNRAS, 442, 844
Fossey, S. J., Cooke, B., Pollack, G., Wilde, M., & Wright, T. 2014, CBET, 3792
Fraser, M., Ergon, M., Eldridge, J. J., et al. 2011, MNRAS, 417, 1417
Freudling, W., Romaniello, M., Bramich, D. M., et al. 2013, A&A, 559, A96
Fryer, C. L., Ruiter, A. J., Belczynski, K., et al. 2010, ApJ, 725, 296
Galbany, L., Hamuy, M., Phillips, M. M., et al. 2016, AJ, 151, 33
Gal-Yam, A., Arcavi, I., Ofek, E. O., et al. 2014, Natur, 509, 471
Gal-Yam, A., Kasliwal, M. M., Arcavi, I., et al. 2011, ApJ, 736, 159
González-Gaitán, S., Tominaga, N., Molina, J., et al. 2015, MNRAS, 451, 2212
Goobar, A., Kromer, M., Siverd, R., et al. 2015, ApJ, 799, 106
Greiner, J., Bornemann, W., Clemens, C., et al. 2008, PASP, 120, 405
Gutiérrez, C. P., Anderson, J. P., Hamuy, M., et al. 2014, ApJL, 786, L15
Gutiérrez, C. P., Anderson, J. P., Hamuy, M., et al. 2017, ApJ, 850, 90
Hamuy, M. 2003a, ApJ, 582, 905
Hamuy, M. 2003b, arXiv:astro-ph/0309122
Hamuy, M., & Pinto, P. A. 2002, ApJL, 566, L63

Hamuy, M., Pinto, P. A., Maza, J., et al. 2001, ApJ, 558, 615
Höflich, P., & Stein, J. 2002, ApJ, 568, 779
Horiuchi, S., Beacom, J. F., Kochanek, C. S., et al. 2011, ApJ, 738, 154
Hosseinzadeh, G., Sand, D. J., Valenti, S., et al. 2017, ApJL, 845, L11
Huang, F., Wang, X., Zampieri, L., et al. 2016, ApJ, 832, 139
Inserra, C., Turatto, M., Pastorello, A., et al. 2012, MNRAS, 422, 1122
Ivezic, Z., Tyson, J. A., Abel, B., et al. 2008, arXiv:0805.2366
Jencson, J. E., Kasliwal, M. M., Johansson, J., et al. 2017, ApJ, 837, 167
Jha, S. W., Foley, R. J., & Skelton, R. 2016, ATel, 9754
Jones, E., Oliphant, T., Peterson, P., et al. 2001, SciPy: Open Source Scientific tools for Python, https://www.scipy.org/
Kalberla, P. M. W., Burton, W. B., Hartmann, D., et al. 2005, A&A, 440, 775
Kangas, T., Mattila, S., Kankare, E., et al. 2016, MNRAS, 456, 323
Kankare, E., Fraser, M., Ryder, S., et al. 2014a, A&A, 572, A75
Kankare, E., Mattila, S., Ryder, S., et al. 2008, ApJL, 689, L97
Kankare, E., Mattila, S., Ryder, S., et al. 2012, ApJL, 744, L19
Kankare, E., Mattila, S., Ryder, S., et al. 2014b, MNRAS, 440, 1052
Kasen, D. 2010, ApJ, 708, 1025
Kasen, D., Röpke, F. K., & Woosley, S. E. 2009, Natur, 460, 869
Kennicutt, R. C., Jr. 1998, ARA&A, 36, 189
Kennicutt, R. C., Jr., Tamblyn, P., & Congdon, C. E. 1994, ApJ, 435, 22
Khazov, D., Yaron, O., Gal-Yam, A., et al. 2016, ApJ, 818, 3
Kochanek, C. S., Shappee, B. J., Stanek, K. Z., et al. 2017, PASP, 129, 104502
Krühler, T., Küpcü Yoldaş, A., Greiner, J., et al. 2008, ApJ, 685, 376
Lauberts, A., Valentijn, E. A., & Observatory, E. S. 1989, The Surface Photometry Catalogue of the ESO-Uppsala Galaxies (Garching bei Munchen, FRG: European Southern Observatory)
Law, N. M., Kulkarni, S. R., Dekany, R. G., et al. 2009, PASP, 121, 1395
Leonard, D. C., Filippenko, A. V., Gates, E. L., et al. 2002, PASP, 114, 35
López-Sánchez, Á R., Dopita, M. A., Kewley, L. J., et al. 2012, MNRAS, 426, 2630
Maguire, K., Di Carlo, E., Smartt, S. J., et al. 2010, MNRAS, 404, 981
Maoz, D., & Mannucci, F. 2012, PASA, 29, 447
Marion, G. H., Brown, P. J., Vinkó, J., et al. 2016, ApJ, 820, 92
Mattila, S., Dahlen, T., Efstathiou, A., et al. 2012, ApJ, 756, 111
Maund, J. R., Smartt, S. J., & Danziger, I. J. 2005, MNRAS, 364, L33
Mazzali, P. A. 2001, MNRAS, 321, 341
Mazzali, P. A., Sullivan, M., Hachinger, S., et al. 2014, MNRAS, 439, 1959
Melinder, J., Dahlen, T., Mencía Trinchant, L., et al. 2012, A&A, 545, A96
Miller, A. A., Cao, Y., Piro, A. L., et al. 2017, ApJ, submitted (arXiv:1708.07124)
Misra, K., Pooley, D., Chandra, P., et al. 2007, MNRAS, 381, 280
Moorwood, A., Cuby, J.-G., & Lidman, C. 1998, Msngr, 91, 9
Muñoz-Mateos, J. C., Sheth, K., Regan, M., et al. 2015, ApJS, 219, 3
Nugent, P. E., Sullivan, M., Cenko, S. B., et al. 2011, Natur, 480, 344
Pastorello, A., Valenti, S., Zampieri, L., et al. 2009, MNRAS, 394, 2266
Pettini, M., & Pagel, B. E. J. 2004, MNRAS, 348, L59
Phillips, M. M., Simon, J. D., Morrell, N., et al. 2013, ApJ, 779, 38
Pignata, G., Benetti, S., Mazzali, P. A., et al. 2008, MNRAS, 388, 971
Pignata, G., Maza, J., Hamuy, M., Antezana, R., & Gonzalez, L. 2009, RMxAC, 35, 317
Pilyugin, L. S., & Mattsson, L. 2011, MNRAS, 412, 1145
Piro, A. L., Muhleisen, M., Arcavi, I., et al. 2017, ApJ, 846, 94
Piro, A. L., & Nakar, E. 2014, ApJ, 784, 85
Poznanski, D., Prochaska, J. X., & Bloom, J. S. 2012, MNRAS, 426, 1465
Pozzo, M., Meikle, W. P. S., Fassia, A., et al. 2004, MNRAS, 352, 457
Quimby, R. M., Wheeler, J. C., Höflich, P., et al. 2007, ApJ, 666, 1093
Rabinak, I., & Waxman, E. 2011, ApJ, 728, 63
Reichart, D., Nysewander, M., Moran, J., et al. 2005, NCimC, 28, 767
Röpke, F. K., Hillebrandt, W., Schmidt, W., et al. 2007, ApJ, 668, 1132
Rosa-González, D., Terlevich, E., & Terlevich, R. 2002, MNRAS, 332, 283
Rubin, A., & Gal-Yam, A. 2016, ApJ, 828, 111
Rubin, A., & Gal-Yam, A. 2017, ApJ, 848, 8
Rubin, A., Gal-Yam, A., De Cia, A., et al. 2016, ApJ, 820, 33
Sahu, D. K., Anupama, G. C., Srividya, S., & Muneer, S. 2006, MNRAS, 372, 1315
Sand, D., Wyatt, S., Valenti, S., et al. 2017a, ATel, 10343
Sand, D. J., Valenti, S., Tartaglia, L., et al. 2017b, ATel, 10569
Sanders, D. B., Mazzarella, J. M., Kim, D.-C., Surace, J. A., & Soifer, B. T. 2003, AJ, 126, 1607
Sanders, N. E., Soderberg, A. M., Gezari, S., et al. 2015, ApJ, 799, 208
Sapir, N., & Waxman, E. 2017, ApJ, 838, 130
Schlafly, E. F., & Finkbeiner, D. P. 2011, ApJ, 737, 103
Schmidt, B. P., Kirshner, R. P., & Eastman, R. G. 1992, ApJ, 395, 366
Schmidt, B. P., Kirshner, R. P., Eastman, R. G., et al. 1994, AJ, 107, 1444
Shappee, B. J., Prieto, J. L., Grupe, D., et al. 2014, ApJ, 788, 48
Simcoe, R. A., Burgasser, A. J., Schechter, P. L., et al. 2013, PASP, 125, 270
Smartt, S. J. 2009, ARA&A, 47, 63
Smartt, S. J., Valenti, S., Fraser, M., et al. 2015, A&A, 579, A40
Smith, K. W., Rodriguez, O., Takats, K., et al. 2016, ATel, 9784
Smith, N., Mauerhan, J. C., Cenko, S. B., et al. 2015, MNRAS, 449, 1876
Spiro, S., Pastorello, A., Pumo, M. L., et al. 2014, MNRAS, 439, 2873
Strolger, L.-G., Dahlen, T., Rodney, S. A., et al. 2015, ApJ, 813, 93
Tartaglia, L., Fraser, M., Sand, D. J., et al. 2017a, ApJL, 836, L12
Tartaglia, L., Hosseinzadeh, G., Arcavi, I., et al. 2016a, ATel, 9453
Tartaglia, L., Sand, D., & Valenti, S. 2016b, ATel, 9782
Tartaglia, L., Sand, D., Valenti, S., et al. 2017b, ATel, 10058
Tartaglia, L., Sand, D., Wyatt, S., et al. 2017c, ATel, 10260
Tartaglia, L., Sand, D., Wyatt, S., et al. 2017d, ATel, 10439
Tartaglia, L., Sand, D., Wyatt, S., et al. 2017e, ATel, 10629
Tartaglia, L., Sand, D., Wyatt, S., et al. 2017f, ATel, 10637
Tartaglia, L., Sand, D., Wyatt, S., et al. 2017g, ATel, 10638
Tartaglia, L., Sand, D., Wyatt, S., et al. 2017h, ATel, 10158
Tartaglia, L., Sand, D., Wyatt, S., et al. 2017i, ATel, 10214
Tonry, J., Denneau, L., Stalder, B., et al. 2016, ATel, 9749
Tonry, J. L. 2011, PASP, 123, 58
Tully, R. B., Courtois, H. M., Dolphin, A. E., et al. 2013, AJ, 146, 86
Vacca, W. D., Cushing, M. C., & Rayner, J. T. 2003, PASP, 115, 389
Valenti, S., Sand, D. J., Yang, S., et al. 2017a, ApJL, 848, L24
Valenti, S., Howell, D. A., Stritzinger, M. D., et al. 2016, MNRAS, 459 3939
Valenti, S., Sand, D., Pastorello, A., et al. 2014, MNRAS, 438, L101
Valenti, S., Sand, D., Stritzinger, M., et al. 2015, MNRAS, 448, 2608
Valenti, S., Tartaglia, L., Sand, D., et al. 2017b, ATel, 10706
Van Der Walt, S., Colbert, S. C., & Varoquaux, G. 2011, CSE, 13, 22
Van Dyk, S. D., Cenko, S. B., Poznanski, D., et al. 2012a, ApJ, 756, 131
Van Dyk, S. D., Davidge, T. J., Elias-Rosa, N., et al. 2012b, AJ, 143, 19
Vernet, J., Dekker, H., D'Odorico, S., et al. 2011, A&A, 536, A105
White, D. J., Daw, E. J., & Dhillon, V. S. 2011, CQGra, 28, 085016
Yang, S., Valenti, S., Cappellaro, E., et al. 2017, ApJL, 851, L48
Yaron, O., & Gal-Yam, A. 2012, PASP, 124, 668
Yaron, O., Perley, D. A., Gal-Yam, A., et al. 2017, NatPh, 13, 510
Zheng, W., Silverman, J. M., Filippenko, A. V., et al. 2013, ApJL, 778, L15